2018

Dynamic topography of passive continental margins and their hinterlands since the Cretaceous

R. Dietmar Muller
University of Sydney

Rakib Hassan
University of Sydney

Michael Gurnis
California Institute of Technology

Nicolas Flament
University of Wollongong, nflament@uow.edu.au

Simon E. Williams
University of Sydney

Publication Details

Muller, R. D., Hassan, R., Gurnis, M., Flament, N. & Williams, S. E. (2018). Dynamic topography of passive continental margins and their hinterlands since the Cretaceous. Gondwana Research, 53 225-251.

Dynamic topography of passive continental margins and their hinterlands since the Cretaceous

Abstract

Even though it is well accepted that the Earth's surface topography has been affected by mantle-convection induced dynamic topography, its magnitude and time-dependence remain controversial. The dynamic influence to topographic change along continental margins is particularly difficult to unravel, because their stratigraphic record is dominated by tectonic subsidence caused by rifting. We follow a three-fold approach to estimate dynamic topographic change along passive margins based on a set of seven global mantle convection models. We first demonstrate that a geodynamic forward model that includes adiabatic and viscous heating in addition to internal heating from radiogenic sources, and a mantle viscosity profile with a gradual increase in viscosity below the mantle transition zone, provides a greatly improved match to the spectral range of residual topography end-members as compared with previous models at very long wavelengths (spherical degrees 2-3). We then combine global sea level estimates with predicted surface dynamic topography to evaluate the match between predicted continental flooding patterns and published paleo-coastlines by comparing predicted versus geologically reconstructed land fractions and spatial overlaps of flooded regions for individual continents since 140 Ma. Modelled versus geologically reconstructed land fractions match within 10% for most models, and the spatial overlaps of inundated regions are mostly between 85% and 100% for the Cenozoic, dropping to about 75-100% in the Cretaceous. Regions that have been strongly affected by mantle plumes are generally not captured well in our models, as plumes are suppressed in most of them, and our models with dynamically evolving plumes do not replicate the location and timing of observed plume products. We categorise the evolution of modelled dynamic topography in both continental interiors and along passive margins using cluster analysis to investigate how clusters of similar dynamic topography time series are distributed spatially. A subdivision of four clusters is found to best reveal end-members of dynamic topography evolution along passive margins and their hinterlands, differentiating topographic stability, long-term pronounced subsidence, initial stability over a dynamic high followed by moderate subsidence and regions that are relatively proximal to subduction zones with varied dynamic topography histories. Along passive continental margins the most commonly observed process is a gradual motion from dynamic highs towards lows during the fragmentation of Pangea, reflecting the location of many passive margins now over slabs sinking in the lower mantle. Our best-fit model results in up to 500 (± 150) m of total dynamic subsidence of continental interiors while along passive margins the maximum predicted dynamic topographic change over 140 million years is about 350 (± 150) m of subsidence. Models with plumes exhibit clusters of transient passive margin uplift of about 200 ± 200 m, but are mainly characterised by long-term subsidence of up to 400 m. The good overall match between predicted dynamic topography to geologically mapped paleo-coastlines makes a convincing case that mantle-driven topographic change is a critical component of relative sea level change, and indeed the main driving force for generating the observed geometries and timings of large-scale continental inundation through time.

Disciplines

Medicine and Health Sciences | Social and Behavioral Sciences

Publication Details

Muller, R. D., Hassan, R., Gurnis, M., Flament, N. & Williams, S. E. (2018). Dynamic topography of passive continental margins and their hinterlands since the Cretaceous. Gondwana Research, 53 225-251.

Dynamic topography of passive continental margins and their hinterlands since the Cretaceous

R.D. Müller[1*], R. Hassan[1], M. Gurnis[2], N. Flament[1,3], S.E. Williams[1]

[1] EarthByte Group, School of Geosciences, University of Sydney, NSW 2006, Australia

[2] Seismological Laboratory, California Institute of Technology, Pasadena, CA, USA

[3] Now at School of Earth and Environmental Sciences, University of Wollongong, Northfields Avenue, Wollongong, NSW 2522, Australia

Submitted to Gondwana Research

* Corresponding author

E-mail: dietmar.muller@sydney.edu.au (R.D. Müller)

Tel: +61 (0) 2 9036 6533; Fax: +61 (0) 2 9351 2442

Abstract

Even though it is well accepted that the Earth's surface topography has been affected by mantle-convection induced dynamic topography, its magnitude and time-dependence remain controversial. The dynamic influence to topographic change along continental margins is particularly difficult to unravel, because their stratigraphic record is dominated by tectonic subsidence caused by rifting. We follow a three-fold approach to estimate dynamic topographic change along passive margins based on a set of seven global mantle convection models. We first demonstrate that a geodynamic forward model that includes adiabatic and viscous heating in addition to internal heating from radiogenic sources, and a mantle viscosity profile with a gradual increase in viscosity below the mantle transition zone, provides a greatly improved match to the spectral range of residual topography end-members as compared with previous models at very long wavelengths (spherical degrees 2-3). We then combine global sea level estimates with predicted surface dynamic topography to evaluate the match between predicted continental flooding patterns and published paleo-coastlines by comparing predicted versus geologically reconstructed land fractions and spatial overlaps of flooded regions for individual continents since 140 Ma. Modelled versus geologically reconstructed land fractions match within 10% for most models, and the spatial overlaps of inundated regions are mostly between 85% and 100% for the Cenozoic, dropping to about 75-100% in the Cretaceous. Regions that have been strongly affected by mantle plumes are generally not captured well in our models, as plumes are suppressed in most of them, and our models with dynamically evolving plumes do not replicate the location and timing of observed plume products. We categorise the evolution of modelled dynamic topography in both continental interiors and along passive margins using cluster analysis to investigate how clusters of similar dynamic topography time series are distributed spatially.

A subdivision of four clusters is found to best reveal end-members of dynamic topography evolution along passive margins and their hinterlands, differentiating topographic stability, long-term pronounced subsidence, initial stability over a dynamic high followed by moderate subsidence and regions that are relatively proximal to subduction zones with varied dynamic topography histories. Along passive continental margins the most commonly observed process is a gradual motion from dynamic highs towards lows during the fragmentation of Pangea, reflecting the location of many passive margins now over slabs sinking in the lower mantle. Our best-fit model results in up to 500 (±150) m of total dynamic subsidence of continental interiors while along passive margins the maximum predicted dynamic topographic change over 140 million years is about 350 (±150) m of subsidence. Models with plumes exhibit clusters of transient passive margin uplift of about 200 ±200m, but are mainly characterised by long-term subsidence of up to 400 m. The good overall match between predicted dynamic topography to geologically mapped paleo-coastlines makes a convincing case that mantle-driven topographic change is a critical component of relative sea level change, and indeed the main driving force for generating the observed geometries and timings of large-scale continental inundation through time.

Introduction

The vertical motions and water depth of passive margins are dominated by the intensity of lithospheric thinning, and sediment accumulation through time (Kirschner et al., 2010). A number of mechanisms have been suggested to account for additional, anomalous vertical motions of passive margins, and many lines of evidence suggest that there is no single mechanism that can account for all observed subsidence and uplift anomalies in this context. Changes in intraplate stresses have been widely inferred to cause flexure, either uplift or subsidence, and inversion along passive margins (Cloetingh, 1988; Lowell, 1995). However, there are few published models for intraplate stress variations through geological time that could be used to predict their effect on basins and margins, and inversion of faults underlying passive margins is also relatively localised. Recently, Yamato et al. (2013) proposed that major changes in mantle convection regimes can induce margin compression and uplift, while Schiffer and Nielsen (2016) investigated the effect of plumes on margin uplift and changes in lithospheric stress in the North Atlantic. Japsen et al. (2012) favoured lithospheric-scale folding at craton boundaries as a universal explanation for anomalous margin uplift, but observations supporting this idea are limited to only a few regions. Braun (2010) reviewed the expressions of mantle dynamic surface topography on continental interiors globally, without specifically investigating the effect on continental margins; this partly reflects that dynamic topographic changes affecting continents are more readily observed in continental interiors far away from geologically recent plate deformation.

Recently, the potential influence of mantle-driven dynamic topography at present-day was analysed in a number of different ways, comparing a variety of observations and assumptions to derive residual, non-isostatic topography with geodynamic model predictions (Hoggard et al., 2016). However, present-day estimates of residual topography alone do not provide insights into dynamic topography affecting continents and their margins through time, as dynamic topography by its nature is time variable. In response to the need to understand the long-term effect of plate-mantle interaction on passive margins, different mantle convection approaches have been developed (e.g. Gurnis, 1993). A widely-used approach for modelling these geodynamic processes in the recent geological past is the inversion of tomographically imaged mantle structure together with other observations to model surface dynamic topography (see Flament et al., 2013, for a review), as recently applied, for example, to the last three million years to the eastern margin of the United States by (Moucha et al., 2008). However, this approach is not useful for modelling these processes through deep geological time, because the current mantle structure does not provide sufficient information to model plate mantle interaction since the breakup of the supercontinent Pangea, in the course of which most current passive margins formed. This issue was recently evaluated in detail by Rowley et al. (2013), who confirmed that retrodictions of mantle flow into deep geological time are possible only if the plate velocity field is used as an additional constraint. It is well established that a plate motion model is needed to model plate-mantle interactions in deep geological time (see recent discussions of the opportunities and limitations of this approach by Colli et al. (2015), as fully dynamic mantle convection models are not yet able to reproduce the evolution of the plate-mantle system realistically; however, recently developed sequential data assimilation methods (Bocher et al., 2016; Colli et al., 2015), currently only tested in 2D simulations, and adjoint methods (Li et al., 2017), hold the promise of more physically realistic plate-mantle models to evaluate the effect of mantle dynamics on surface topography.

In order to overcome some of these current methodological limits, a geodynamic forward modelling approach with time-dependent slab assimilation constrained by a global tectonic model has been developed (Bower et al., 2015). This method has been applied previously to investigate the role of mantle convection in driving large-scale (> 1000 km wavelength) anomalous subsidence or uplift of passive margins in a number of regions including the east coast of North America (Flament et al., 2013), the South Atlantic domain (Flament et al., 2014), the Arctic (Shephard et al., 2014), Southeast Asia (Zahirovic et al., 2016), northern Africa (Barnett‐Moore et al., 2017) and the east Australian margin (Müller et al., 2016).

However, this approach has not yet been evaluated in the context of a global analysis of the influence of large-scale mantle flow on the subsidence and uplift of passive margins and their hinterlands through time. This partly reflects the difficulties in comparing the output of global mantle dynamic flow models with detailed local observations from continental margins, either based on present-day residual topography analysis (Hoggard et al., 2016) or stratigraphic data from wells providing estimates of tectonic subsidence or uplift anomalies through time (e.g. Xie et al., 2006). Currently observed residual topography may reflect several processes other than large-scale mantle convection, including lithospheric thickness and/or density anomalies (e.g. Xie et al., 2006), as well as asthenospheric temperature anomalies and small-scale convection (Pedersen et al., 2016), complicating its interpretation. Similarly backstripped tectonic subsidence derived from individual wells may be influenced by local tectonic reactivation and faulting processes (e.g. Colli et al., 2014; Hoggard et al., 2016), in addition to subsidence following rift-related lithospheric thinning, partly obscuring dynamic topography signals from large-scale mantle convection ((e.g. Johan and Kleinspehn, 2000) for a discussion of the interaction of these signals in the South China Sea). Because of the difficulties in assessing the effect of deep mantle convection-driven dynamic topography for passive continental margins directly, we follow a three-fold approach here. We first analyse the power spectra of a set of seven alternative mantle convection models in the context of the spectra of residual topography end-members to establish their relationship at long wavelengths, and then combine global sea level estimates (Fig. 1) with predicted surface dynamic topography (Figs 2-4) to evaluate modelled continental inundation as compared with published paleo-coastlines through time. Subsequently, we use an established cluster analysis approach to investigate the time-dependent dynamic topography evolution predicted for continental interiors and passive margins by our models.

Methods

Plate reconstructions

We model global mantle flow based on the subduction and plate motion histories predicted by topologically-evolving plate boundaries from three alternative plate reconstructions (Gurnis et al., 2012; Müller et al., 2016; Seton et al., 2012). We use the reconstruction by Müller et al. (2016) as reference, because it includes many recent improvements to our model of regional relative plate motions and plate boundary evolution, including revised maps of the evolution of the age-area distribution of the ocean floor through time, providing improved constraints for the age and thus thickness of subducting oceanic lithosphere through time, a key constraint for assimilating subducting lithosphere into mantle convection models. We also use the reconstruction by Seton et al. (2012) as it has been the reference plate tectonic model for post-Pangea geodynamic modelling for the last few years, providing an opportunity to evaluate the different choices for absolute plate motion models that were made by Seton et al. (2012) versus Müller et al. (2016), especially considering that in the latter model episodes of large global RMS plate velocity, net rotation, and trench migration were minimised to reduce potential artefacts in forward geodynamic models. The tectonic reconstruction by Gurnis et al. (2012), an earlier version of the tectonic reconstruction by Seton et al. (2012) for the last 140 million years, is used to evaluate the predictions of the mantle flow models by Spasojevic and Gurnis (2012) for the last 90 million years.

Geodynamic models

Our calculations begin at 230 Ma in all models with the exception of that by Spasojevic and Gurnis (2012), but we only analyse mantle evolution from the Early Cretaceous (140 Ma) since it takes at least 50 million years for the models to reach an equilibrium from the initial condition (Flament et al., 2014), and because published digital paleo-coastline maps are available only for the period after 140 Ma. The earlier period of forward integration is avoided in Model M1, a hybrid model (Spasojevic and Gurnis, 2012), as the initial global mantle temperature field at present-day is estimated through a combination of seismic tomographic inversions of surface and body waves using model S20RTS (Ritsema et al., 2004) in the lower mantle and one based on Benioff zone seismicity for the upper mantle seismicity. This temperature field is integrated backward using the SBI (simple backward integration) method of Liu and Gurnis (2008) back to the Late Cretaceous by reversing the direction of gravity and plate motions. A hybrid paleo-buoyancy field is generated by merging the backward-advected mantle temperature field with synthetic subducted slabs assimilated into the model based on the location of subduction zones, the age of the subducted lithosphere and relations among subduction zone parameters (Spasojevic and Gurnis, 2012). In all other models analysed here viscous mantle flow is driven in forward models by thermal convection with plate velocities applied as surface boundary conditions, extracted in 1 million year intervals from the plate reconstructions (Bower et al., 2015). The initial condition in models M2-M4 without plumes includes a basal thermochemical layer 113 km thick just above the core–mantle boundary (CMB) that consists of material 4.2% denser than ambient mantle, while in model M7 this layer is 10% denser than ambient mantle. This condition effectively suppresses plumes in the model within the time frame covered by our model runs. This setup prevents the formation of upwelling mantle plumes, making it possible to study the interaction of moving continents with subduction-driven mantle downwellings and the associated large-scale mantle return flow in the absence of individual plumes. The initial condition for models with plumes features a basal chemical layer 100 km thick that is 2.5% heavier than the ambient mantle, embedded in a 300 km thick thermal boundary layer - see Hassan et al. (2015) for a more detailed description of the model setup. The thickness of the thermal lithosphere, derived from the age of the oceanic lithosphere and tectono-thermal age of the continental lithosphere, is assimilated into the dynamic model. We use a modified version of the finite element code CitcomS to obtain one-sided subduction, in which the shallow portion of subducting slabs is imposed to a maximum depth of 350 km, below which mantle convection arises dynamically from prescribed time-dependent conditions (Bower et al., 2015). In models M2-M7 air-loaded dynamic topography is calculated from the surface vertical stress resulting from mantle flow in restarts of the main model run in which the surface boundary condition is free-slip and the 350 km uppermost part of the mantle do not contribute to the flow, while lateral viscosity variations are preserved in the whole mantle. In contrast, in model M1 dynamic topography is computed using a no slip surface boundary condition, and only the top 250 km of the mantle are excluded from contributing to surface topography, which partly explains the somewhat greater amplitude of dynamic topography in model M1 as compared to models M2-M7 (see also Flament et al., 2014; Thoraval and Richards, 1997). Finally, the use of models based only on forward calculations versus those through inversion using seismic constraints allows us to evaluate the role of initiation conditions and fits to present-day seismic structure.

The Rayleigh number that determines the vigour of convection is defined by

$$Ra = \frac{\alpha_0 \rho_0 g_0 \Delta T h_M^3}{\kappa_0 \eta_0},$$

where α is the coefficient of thermal expansion, ρ the density, g the acceleration of gravity, ΔT the non-adiabatic temperature change across the mantle, h_M the depth of the mantle, κ the thermal diffusivity, and η the viscosity in which the subscript "0" indicates reference values. Key model parameters are listed in Table 1.

The average model resolution, obtained with ~13 x 10^6 nodes and radial mesh refinement, is ~ 50 x 50 x 15 km at the surface, ~ 28 x 28 x 27 km at the core–mantle boundary (CMB), and ~ 40 x 40 x 100 km in the mid-mantle. The modelled dynamic topography through time is computed in the mantle and plate frames of reference for models M1-M7, exploring the parameter space in terms of the alternative plate reconstructions and in assumed mantle viscosities (Table 1). In models M2-M4 temperature and thermal expansion are constant with depth and the dense basal layer has the same thickness as the lower thermal boundary layer. In models M5-M7 thermal expansion decreases with depth, the average mantle temperature increases with depth (adiabat) and the dense basal layer is thinner than the lower thermal boundary layer. In models M2-4, the viscosity varies by 1000 due to temperature-dependence following

$$\eta(T, r) = A(r)\eta_0 \exp\left(\frac{E_\eta}{T+T_\eta} - \frac{E_\eta}{T_b+T_\eta}\right),$$

where r is the radius, where $A(r)$ is the pre-exponential parameter for four layers (Table 2), E_η is the non-dimensional activation energy (E_{UM} = 9 in the upper mantle and E_{LM} = 3 in the lower mantle, see Table 2 for dimensional values), T is the temperature, T_η =0.16 is a temperature offset, and T_b = 0.5 is the ambient mantle temperature (see Table 2 for dimensional values). A similar viscosity parameterization is employed in model M1 (Table 2). In models M5-7, we use piecewise Arrhenius laws to describe the variation of viscosity with temperature and depth, which takes the following form:

$$\eta(T,r) = A(r)\eta_0 exp(\frac{E_\eta(r) + (1-r)V_\eta(r)}{T+T_\eta} - \frac{E_\eta(r) + (1-r_{inner})V_\eta(r)}{1+T_\eta}),$$

where V_η is the non-dimensional activation volume. For the lower mantle, we use a dimensional activation energy of 320 $\mathrm{KJ\ mol^{-1}}$ and activation volume of 6.7 X 10^{-6} $\mathrm{m^3\ mol^{-1}}$, corresponding to non-dimensional units of 11 and 26, respectively, which are comparable to estimates (Karato and Wu, 1993). However, since such viscosity parameterizations lead to large viscosity variations that cause numerical difficulties, we adjust the pre-exponential parameter $A(r)$ and the temperature offset T_η (Tackley, 1996) to limit the viscosity contrast to 3 orders of magnitude. The resulting viscosity profile is similar to the preferred viscosity profiles of Steinberger and Calderwood (2006). Models M5-M7 also assume an *a priori* mantle adiabat with top and bottom thermal boundary layers featuring a temperature drop of 1225 K and the initial adiabatic temperature profile has a potential temperature of 1525 K. Moreover, models M5-7 incorporate viscous dissipation and adiabatic heating through the extended Boussinesq approximation (c.f. Christensen and Yuen, 1985; Ita and King, 1994), in addition to internal heating from radiogenic sources. The Boussinesq and Extended Boussinesq Approximations (BA and EBA, respectively) assume an incompressible mantle, while the Anelastic Liquid Approximation (ALA), not utilized here, is used to model mantle compressibility (Ita and King, 1994). However, unlike in the BA, models based on the EBA allow for the inclusion of a pre-calculated thermodynamic model, featuring depth profiles for adiabatic temperature, thermal expansivity and density – see Ita and King (1994) for more detail. We apply a non-dimensional internal heat generation rate of 100 in these model cases and compute a reference profile for thermal expansion, α, based on analytical parameterizations of Tosi *et al*. (2013), using the *a priori* mantle temperature profile. Additional details on the setup of models M5-M7 can be found in Hassan *et al*. (2015).

Model power spectra

We use spherical harmonic analysis to analyse the spectral characteristics of our global dynamic topography models at present-day for spherical harmonic degrees 1-5, and compare them with two end-member spectra of oceanic residual topography from Hoggard et al. (2016, Fig. S2), which capture one of the main sources of uncertainty in computing oceanic residual topography, the flattening of old ocean floor (Fig. 5). The end member spectra are based on Crosby and McKenzie's (2009) plate model (PM) and a thermal boundary layer (TBL) model fitted to ocean floor less than 70 million years in age (Fig. S2 of Hoggard et al. (2016). These residual topography models are well suited to evaluate the amplitudes of long-wavelength dynamic topography as we expect long-wavelength dynamic topography predicted from mantle convection models to fall within the residual topography implied by a plate model and a thermal boundary layer model. This is based on the consideration that plate models potentially overestimate the flattening of old ocean floor, as the observed flattening in at least some regions may be due to deep mantle convection-driven dynamic topography, while thermal boundary layer models underestimate it (see Stein and Stein, 2015, for a recent review). Estimates of continental residual topography are much more uncertain (Yang and Gurnis, 2016), reflecting the considerable heterogeneity of continental lithosphere in terms of its temperature, density and thickness, and not used here.

Paleogeography models

In order to evaluate modelled surface dynamic topography against geologically mapped paleogeography we use two alternative sets of published digital paleo-coastlines (Golonka, 2007, 2009; Smith et al., 1994) for the period 140-0 Ma, which have been rotated into present-day coordinates (Heine et al., 2015) to allow adaptation to different plate models with ease. We interpolate these paleo-coastlines into discrete paleogeographic maps that delineate the distribution of land and water by first generating points on the sphere that sample equal areas (Gorski et al., 2005) in order to produce binary maps (land or marine) for any given paleo-coastline configuration that is taken to be representative for a certain geological time interval (Heine et al., 2015). We then compute the intersection P of binary maps for a given pair of consecutive time-slices (S_{t-1}, S_t). This intersection is a collection of isolated patches that represent regions being submerged, P_w, or becoming emergent, P_l, from time S_{t-1} to time S_t that is, $P = P_w \cup P_l$. We then compute a distance map of P to closest land in S_t, based on a spherical distance metric and normalize the distance map such that within each isolated patch distances range between [0, 1] and relate normalized time progressions between S_{t-1} and S_t to the normalized distance map. In other words, as time progresses between times S_{t-1} and S_t, regions featured in the distance map morph from their former state in S_{t-1} to their subsequent state in S_t, based on corresponding values of distances. These transitions proceed such that regions in P_w farthest from land are inundated first, whereas regions in P_l closest to land emerge first. In the absence of detailed continental paleo-elevation constraints, we assume a linear progression of transgressions and regressions, and obtain interpolated paleogeographic maps at one million year intervals. In the following, we refer to these as paleogeographic models, to differentiate them from geodynamic models.

Model topography versus continental paleogeography through time

The observed present-day topography includes dynamic topography, but given the large uncertainties in both estimates of amplitudes of continental residual topography as well as dynamic models (see recent extensive review by Guerri et al., 2016) we depend on using a simple empirical approach to be able to compare our modelled dynamic topography with mapped paleo-coastlines. The dynamic topography from our models cannot be used in its raw form here, reflecting uncertainties in dynamic topography amplitudes as a consequence of our still limited knowledge of mantle physical properties and chemical composition (Guerri et al., 2016).

We compare the distribution of land and sea in continental regions predicted by global convection models with those from geologically mapped paleo-coastlines (Heine et al., 2015) (except Antarctica), based on a methodology similar to that outlined in Gurnis (1993). We define a 'continent function', $C(t, \theta, \varphi)$, which is a binary map representing the locations of continents through time *t* and space (θ, φ). At each time instance t, we apply the 'continent function', as a mask to the modelled dynamic topography to obtain continental dynamic topography $h(\theta, \varphi)$. Since the geodynamic models presented in this study exclude a significant portion of the upper mantle – ranging from 250 to 350 km from the surface – while computing dynamic topography, the contribution of shallow mantle processes and the spatial variability of lithospheric thickness toward modulating the computed long-wavelength dynamic topography cannot be modelled. Consequently, the mean computed dynamic topography within individual continents (Fig. 6), at any given time, tends to be discrepant with geological observations. As a simple remedy, we remove the mean dynamic topography within each continent from $h(\theta, \varphi)$, which is a reasonable approach given the current limitations of the models. We then derive binary maps of continental inundation patterns based on the inequality below:

$$h(\theta, \varphi) < S(t) + h_c$$

where h_c is a constant and $S(t)$ is the independently derived eustatic sea-level at the time (Fig. 1), taken alternatively from Spasojevic and Gurnis (2012), whose sea level curve is based on Müller et al.'s (2008) ocean basin volume estimates, or from sea level curves based on revised age-area distributions in the ocean basins and revised changes in continental area through time for the last 140 million years from Seton et al. (2012) and Müller et al. (2016), including the same approach used in Müller et al. (2008) to account for the effect of oceanic plateaus and deep-sea sediment thickness through time. These estimates are combined with the mean oceanic dynamic topography effect of a given geodynamic model through time (Fig. 7). We do not consider the effect of mean continental dynamic topography on global sea level change (Gurnis, 1993; Conrad and Husson, 2009; Spasojevic and Gurnis, 2012), and do not attempt to calculate gravitationally self-consistent sea level changes (Austermann and Mitrovica, 2015; Spasojevic and Gurnis, 2012) back in time, due to our currently lacking ability to construct paleo-digital continental elevation models that are corrected for lithospheric thinning and thickening, erosion and sedimentation back to 140 Ma. The choice of ocean volume-derived sea-level curve depends on which plate tectonic model a given geodynamic model is based on. For both the sea level curves based on Seton et al.'s (2012) and Müller et al.'s (2016) oceanic age-area distribution through time, we include the long-term fluctuations in global sea-level from varying continental ice volume since 38 Ma, derived from a zonally averaged energy balance climate model bi-directionally coupled to a one-dimensional ice sheet model (Stap et al., 2016). This approach implies that the continental ice volume between the Early Cretaceous and the Eocene was negligible. There is evidence for the existence of a 5 million year long glacio-eustatic low-stand in the mid-Cretaceous from the flooding record of the Arabian Plate (Maurer et al., 2013) which is not included in our long-term sea level curve. We do not make any ice-volume related adjustment to the sea level curve used by Spasojevic and Gurnis (2012), because eustatic sea level and the regionally fluctuating dynamic topography are self-consistently derived from their geodynamic model and we prefer to retain the relationship between eustasy and dynamic topography as used in their model M5 (here model M1).

In the inequality used to derive continental inundation patterns, the constant h_c is empirically constrained for each convection model separately, such that the spatial extent of predicted flooding in the Early Cretaceous (or Late Cretaceous for model M1) is comparable to those inferred in the paleogeographic maps. This simple empirical approach enables us to generate rough estimates of the flooding of continents through time by combining dynamic topography and eustasy. Long wavelength, space-time varying dynamic topography lows are thus adopted as proxies for shallow marine seas that may arise when continents travel above regions where subducted slab material sinks in the mantle, modulated by global sea level fluctuations.

We compute the fraction of land through time, $\tau(t)$, for each continent, as predicted by the convection models with those from two alternative sets of paleogeography grids (Golonka, 2007, 2009; Smith et al., 1994) derived from the digital paleo-coastlines in Heine et al. (2015) (Figs 8-10b, Supp. Figs 6-9b). Land fractions computed for predictions from the convection models are based on the present-day boundaries between continental and oceanic crust (COB) (Müller et al., 2016), while those computed for the paleogeography grids are based on paleo-coastlines. Thus, in order to make meaningful comparisons between these derived land fractions, we normalize each curve by their corresponding maxima, considering that paleo-coastlines record maximum flooding through time. We further compute similarity coefficients through time, $\mu(t)$, which show the degree of spatial overlap of the distribution of land or ocean between model predictions and the two sets of paleogeography grids. The similarity coefficients are also normalized – for similar reasons – by their corresponding maxima, and we refer to this measure in the following as inundation overlap.

We evaluate the overall quality of our models by computing the difference between similarity coefficients for geodynamically modelled and geologically mapped continental inundation, given in terms of land fraction differences, for individual continents as well as the root mean square difference averaged for all continents. These measures highlight whether the models over- or underestimate inundation for individual continents, and summarise the overall performance of a given model to match geologically mapped inundation through time. These statistics are computed for three time periods, i.e. 0-60 Ma, 60-100 Ma (90 Ma for M1) and 100-140 Ma, roughly representing the Cenozoic, Late and Early Cretaceous periods, considering that model matches to continental inundation patterns tend to vary significantly between these periods. In addition we compute the overlaps between our model inundation predictions for individual continents and time periods and geologically modelled inundation patterns. This measure reveals to what extent predicted continental inundation overlaps spatially with geologically mapped inundation, and is a useful measure in addition to land fraction similarities.

Cluster analysis of dynamic topography

We use a *k-means* clustering algorithm (Lloyd, 1982) to obtain objective classifications of geographic regions that share similar uplift and subsidence histories, predicted by the geodynamic models. The *k-means* algorithm partitions data items into k clusters such that the sum of the distances over the data items in each cluster to their cluster centre is minimal, i.e., given a set of observations ($x_1, x_2, \ldots, x_n$), where each observation can be d dimensional, the algorithm partitions the n observations into $k(\leq n)$ sets S. In our case, each observation x_i is a time-series of dynamic topography estimates at a given location; each set S_i identifies localities on continents that share a common uplift and subsidence history. It should be noted that k, the number of clusters, is chosen *a priori* and we chose a range of values of k to draw out dominant trends within dynamic topography predicted by our mantle convection models. The resulting cluster maps (Figs. 11-12) represent an objective regional summary of dynamic topography trends through time as predicted by a range of geodynamic models based on different plate tectonic models, mantle rheologies and other parameters described in the geodynamic modelling methodology section. We further separately analyse continental passive margins, including all passive margins irrespective of their age, using bands of a fixed width of 200 km. We include the dynamic topography history preceding continental rifting for margins younger than 150 Ma.

Results

Model power spectra

Models M1-4 overestimate oceanic residual oceanic topography at degrees 1-3, while the power of models M5-7 at degrees 2-3 is within the range of end-member values based on a plate versus thermal boundary layer model (Fig. 5). M5-M7 display more power at degree 1 than M2-M4, and M1 displays the most power at degrees 1-3 amongst all models used here. In models M5-M7, the Pacific region features a strong “superplume”-like upwelling not found in the Indo-Atlantic (Supp. Fig. 5). This pronounced large-scale Pacific upwelling corresponds low seismic velocities in mantle tomography (French and Romanowicz, 2015). The degree 1 spherical harmonic (Supp. Fig. 5) captures this Pacific upwelling and becomes dominant in the power spectrum. This is the case even in model M7 with an initial 10% denser basal thermochemical layer that suppresses the formation of mantle plumes; but even here, the large-scale Pacific upwelling is more pronounced than in the Indo-Atlantic. As a consequence, the degree 1 spherical harmonic that captures the sub-Pacific upwelling becomes dominant in the power spectrum. It is important to note that this degree 1 peak driven by a Pacific “superplume” does not influence our results for the continents, which do not intersect its periphery, with the exception of the western portion of South America and eastern Australia (Supp. Fig. 5), with the latter having experienced renewed uplift of its eastern highlands in the Late Cenozoic perhaps due to overriding the edge of this upwelling (Müller et al., 2016).

The r.m.s. amplitude of model M7, as a representative case of models M5-M7, at degree 1 is 1050 m, while end member residual topography models (Fig. 5) yield 350m (TBL) and 270m

(PM), mainly illustrating that the amplitude of large-scale Pacific mantle upwelling is overestimated. However, at degree 2, the r.m.s. amplitude of model M7 is 740 m, within the range of residual topography end-members at 850 m (TBL) and 530 m (PM). At degree 3, the r.m.s. amplitude of M7 is 570 m, also within a plausible residual topography range of 770 m (TBL) and 510 m (PM). This analysis indicates that model M7, as well as M5-6, yield dynamic topography amplitudes which are consistent with observations at long wavelengths, with the exception of degree 1, making them promising candidates for understanding continental inundation through time. In models M5-7 viscous heating causes slab interiors to weaken over timescales of a few million years (e.g. Larsen et al. (1995). Consequently, the negative dynamic topography associated with sinking slabs diminishes with the warming of slab material during its descent in the mantle. Although the models here have unrealistically high amplitudes at degrees 1-3, by adjusting the mean of individual models, as outlined above, we ensure that models can be used to investigate the role of dynamic topography on continental inundation patterns through time.

Geodynamically modelled continental inundation versus paleogeography

We evaluate the combination of predicted dynamic surface topography jointly with eustatic sea level curves based on modelled ocean basin volumes from the plate model that was used as surface boundary condition for a given geodynamic model combined with the oceanic dynamic topography predicted by the same geodynamic model (Figs 2-4; supp. Figs 1-4) with regard to their match to published paleo-coastline locations in a plate reference frame (Figs 8a-10a; supp. Figs. 6a-9a), first in terms of predicted versus geologically mapped land fractions through time and similarities in the degree of spatial overlap of the distribution of submerged continental regions between model predictions and the two sets of paleogeography grids (Figs 8b-10b; supp. Figs. 6b-9b).

Geodynamic model M1 (Fig. 2), based on combined backward advection models of the present-day mantle structure and forward subduction modelling (Spasojevic and Gurnis, 2012), matches the two paleogeography models for the Cenozoic compared here (Golonka, 2009; Smith et al., 1994) fairly well for North and South America, while somewhat less well for the land fractions and inundation overlaps of other continents (Fig. 8b); the overall fit of this model to either paleogeography deteriorates somewhat from the Cenozoic into the Late Cretaceous (Fig. 8b). However, the trend of increased inundation (decreased land fraction) of both Americas, and to some extent Eurasia, from the Early Cenozoic back into the Late Cretaceous is well captured by this model (Fig. 8b). For the Cenozoic, inundation overlaps for model M1 are similar for both paleogeographic reconstructions (Golonka, 2009; Smith et al., 1994), while for the Late Cretaceous period (~100-65 Ma) the two reconstructed paleogeographies diverge more significantly from each other (Fig. 8b). Generally, this results in a better agreement of the geodynamic model with Golonka's (2007) model than with Smith et al.'s (1994) model before 65 Ma, with the exception of North America (Fig. 8b), where this order is reversed.

Next we evaluate the predicted dynamic topography through time from three forward geodynamic models (M2-4) driven by alternative plate models (Fig. 3, supp. Figs 1 and 2). In terms of modelled land fractions and inundation patterns, models M3 and M4 fit South America relatively well, but only for Golonka's paleogeography (Golonka, 2007, 2009) (Fig. 9, Supp. Figs 6b, 7b). The good fit in this region reflects the modelled inclusion of inferred episodes of flat slab subduction along South America (Flament et al., 2015). Model M2 (Supp. Fig. 6b) based on the older (Seton et al., 2012) reconstruction, fits less well, partly reflecting its reduced global sea level amplitude compared with the two other two models (Müller et al., 2008; Müller et al., 2016) as well as a different history of the age of subducting crust through time along the Andes. The evolution and eastward migration of the western interior seaway in North America (Liu et al., 2014), reflecting the effect of the Laramide flat slab (English et al., 2003) on surface dynamic topography, is moderately well captured in these geodynamic models, but again only as compared with Golonka's paleogeography. However, in these geodynamic models North America remains excessively flooded in the early-mid Cenozoic (Fig. 9b), likely reflecting that Laramide slab breakoff and sinking into the lower mantle (potentially resulting in surface rebound) is not appropriately captured in these models.

Models M2-M4 capture Eurasia's flooding history relatively well over the Late Cenozoic, but tend to underestimate flooding in the Early Cenozoic, likely reflecting the complex tectonic history of Eurasia that results in regional flooding not accounted for in our models. Even though the modelled Cretaceous land fractions match Golonka's paleogeography Golonka (2007) for Eurasia, the inundation overlaps are generally not better than 80% for and between 65 and 75% for Smith et al. (1994) (Fig. 9b). Africa's land fraction is poorly matched for this entire set of models (Fig. 9b, Supp. Figs 6b, 7b). For Australia, models M2-4 underestimate Cenozoic flooding of Australia, likely reflecting shortcomings in the modelled subduction history around Australia in all plate models used here. The early Cretaceous flooding followed by Late Cretaceous rebound is generally captured with a 5-15 Myr time lag depending on the plate motion model used (Fig. 9b, Supp. Figs 6b, 7b). Both subduction zone locations east of Australia as well as the absolute plate motion interaction between Australia and sinking slabs in the mantle depend on particular plate models (see Müller et al. (2016) for discussion).

Models M5-7, being forward subduction models like models M2-4, but with a pressure-dependent viscosity structure that involves a more gradual increase in viscosity between the upper and lower mantle and uses an extended Boussinesq approximation, are characterized by somewhat smaller amplitudes in surface dynamic topography (e.g. see M7, Fig. 4). In addition, models M5 and M6 both include plumes, but their exact location and arrival time at the surface cannot be controlled as the plumes develop dynamically in the lower mantle (Supp. Figs 3, 4). As a consequence, continents that are affected by model plumes through time, particularly Africa and Australia (M5 and M6) show different and sometimes unrealistic inundation patterns (Supp. Figs 8b, 9b) compared with model M7, in which plumes are suppressed (Fig. 10). Hassan et al. (2015) demonstrated that in model M5 (identical to their model M3) that plumes arise in locations near to present day hot spot locations at a statistically significant level. However, the exact arrival time and location of a given plume head at the surface as well as the subsequent lateral plume motion or tilt is dynamic rather than imposed, resulting in a variable match with geological observations. Model M5, characterised by the evolution of an Afar-like plume (Fig. 4), results in the most reasonable Cenozoic flooding history of Africa amongst all the geodynamic models analysed here (Fig. 10b), while the opposite holds for Australia, where the evolution of model mantle upwellings in M5 worsens the fit to paleogeography (Fig. 10b). In contrast, matches between geodynamic model predictions with paleogeography for Cenozoic Eurasia are relatively unaffected by the presence or absence of plumes (Fig. 10b), reflecting that most of continental Eurasia is not affected by mantle plumes since the Cretaceous. However, it is worth noting that all seven geodynamic models perform poorly in terms of Cretaceous patterns of inundation in Eurasia, partly reflecting Eurasia's tectonic complexity (De Grave and Buslov, 2007). Model M7, in which plumes are suppressed, results in the best overall matches to continental flooding amongst models M5-7 (Fig. 10b), with the exception of Africa.

Reconstructed paleo-coastlines not only reflect eustasy and dynamic topography, but also lithospheric thickening and thinning, factors not considered in the forward models. Because of this, continental inundation models display short- to medium-wavelength mismatches with geologically-reconstructed coastlines, and this is reflected in improved model fits for relatively stable continents (like North America) versus continents that have experienced numerous orogenies and rifts (like Eurasia).

Clusters of dynamic topography evolution

The long-term evolution of continental dynamic topography is primarily driven by their interaction with sinking slabs and large mantle upwellings away from slabs, which represent the large-scale vertical return flow in response to subduction. During the breakup of Pangea and the subsequent dispersal of continents, some continental regions have remained in the vicinity either of a large upwelling (associated with an LLSVP) or of "neutral" mantle away from both large upwellings and subduction zones (Figs 2-4). In these cases continental regions have experienced little change in dynamic topography. In contrast, many other continental regions have moved over subducting slabs after the breakup of Pangea, resulting in these regions being drawn down at least in a particular period during dispersal, affecting both regional as well as global sea level. Some regions are still overlying "slab burial grounds", while others have moved across subducting slabs and have experienced a change from dynamic subsidence to uplift. There are also regions that have mainly experienced distinct dynamic uplift by either being over a plume at certain time intervals (in those models that include plumes) or by moving towards a large mantle upwelling (sometimes referred to as superplumes) (Figs 2-4). Cluster analysis allows us to segment continental regions into different classes of dynamic topography evolution, but the most appropriate number of classes is not known *a priori*. We explore 3-5 clusters for all continental regions, and then repeat the same analysis for passive margin regions only to assess the differences in which continental interiors and passive margins may have been affected by mantle-driven dynamic topography.

Different groups of geodynamic models naturally yield different categories of clusters. For instance, models M5-7 differ substantially from all other models, with M5 and M6 moreover including plumes, which are suppressed in models M2, M3 and M7, while model M1 may contain active upwellings assimilated from the S20RTS mantle tomography model (Ritsema et al., 2004). Based on these differences, some models display evolutionary paths of dynamic topography that are not common in others. Considering three clusters demonstrates that this number insufficiently captures the diversity of dynamic topographic evolution of continental regions, with the exception of M1 (Fig. 11), partly reflecting that this model only covers a 90 million year time period. Here three clusters differentiate topographic stability from long-term subsidence in regions overlying slab burial grounds for the entire model period as well as long-term subsidence in more elevated regions initially more distal to subduction zones, but gradually moving over sinking slabs (Fig. 11).

For all other models, a choice of four clusters (Fig. 12) differentiates topographic stability, long-term pronounced subsidence, initial stability over a dynamic high followed by moderate subsidence and a fourth cluster representing regions proximal to subduction zones, either with initial subsidence followed by uplift (M2-4), or accelerating subsidence through time (M5-7) (Table 3). We find that using five clusters does not add improve the categorisation of continental dynamic topography evolution. In terms of the maximum amplitude of total dynamic topographic change over 140 million years, our favoured model M7 results in up to 500 (±150) m of total dynamic subsidence (TDS) (cluster 1) while the other clusters are limited to total change of the order of 200-300 m (Fig. 12), reflecting that the long-term dynamic topographic change effect in most continental regions is within the range of first-order eustatic sea level fluctuations for this model (Fig. 1). The subsidence clusters in Model M1 result in a maximum of 350 (±200) m of TDS over 90 million years (Fig. 11), of a similar order of magnitude to model M7, while the subsidence cluster in models M2-4 typically results in TDS of 1000 (±400) m, which is significantly larger than estimated eustatic sea level fluctuations over this time period (Fig. 1), reflecting that this class of models may overestimate negative dynamic topography.

The four-cluster categorisation of dynamic topography through time as described for the continents is mirrored by continental margins (Fig. 13), exhibiting similar evolutionary paths. The most commonly observed process is a gradual move of passive margins from dynamic highs towards dynamic lows during Pangea fragmentation, reflecting that many continental passive margins now overlie slabs sinking in the lower mantle. This holds for portions of the eastern margins of North (Spasojevic et al., 2008) and South America (Flament et al., 2014), northern Africa (Barnett‐Moore et al., 2017) as well as some segments of Australia's margins, particularly the northeast (DiCaprio et al., 2010), while the margins of eastern Brazil, South Africa as well as southwest Australia are examples where dynamic stability or uplift is predicted in most of our models (Fig. 13). For passive margins, the maximum predicted dynamic topographic change over 140 million years in model M7 is about 350 (±150) m of subsidence, about an order of magnitude smaller than the total tectonic subsidence (Sawyer, 1985) typically caused by rifting, making dynamic signals difficult to detect in tectonic subsidence analyses based on borehole stratigraphy, especially considering typical uncertainties in paleo-water depth (Allen and Allen, 2013). The subsidence clusters in model M1 result in a maximum of 400 (±200) m of TDS over 90 million years (Fig. 11), while the subsidence cluster in models M2-4 results in TDS of 1000 (±400) m, similar to estimates for all continents (Fig. 13).

In a model in which plumes are suppressed, such as M7, passive margins exhibit a more pronounced tendency to be affected by uplift than continental interiors, but the mean amplitude of this effect is of the order of 100 ±50m (M7, cluster 4, Fig. 13). In models M2-M4 the magnitude of this effect along passive margins is as large as ~500±300m (model M3), and there are instances, like southeast Australia, where Cenozoic dynamic uplift of about 500 m is supported by river profile inversion (Czarnota et al., 2014). Models with plumes result in transient passive margin uplift of about 200 ±200m (e.g. M6, cluster 4, Fig. 13), but are mostly characterised by long-term subsidence. A region in which plume-related Late Cenozoic dynamic uplift as modelled in M6 (Fig. 13) is promising in terms of its match to observations is the north eastern Brazilian Borborema Province, where post 50 Ma magmatic plugs have been interpreted as Brazil moving over a hotspot (Mizusaki et al., 2002). Similarly, Late Cenozoic uplift of the south African margin (Roberts and White, 2010) is captured in this model. A detailed comparison of tectonic subsidence derived from exploration wells with our geodynamic models is beyond the scope of this paper. However, we provide interactive geodynamic model access via the GPlates Portal (portal.gplates.org, Müller et al., 2016), where end users can easily extract the predicted dynamic history for any given site, for any of the models presented herein, download the data and evaluate their match with any given tectonic subsidence history.

Discussion

Before discussing our results for the dynamic topography for passive margins and their hinterlands through time, we first review model predictions for present-day dynamic topography. Residual oceanic basement depth is perhaps the most useful present-day validation of surface dynamic topography, given the much larger uncertainty of estimating continental residual topography (Colli et al., 2016; Yang and Gurnis, 2016), but it is dependent on a number of assumptions related to the depth-age relationship of "normal" ocean floor (see recent review by Stein and Stein, 2015). Even though oceanic depth-age models are typically constructed by excluding data from hotspot swells (see for instance Crosby and McKenzie, 2009), they are based on the assumption that long-wavelength dynamic topography does not exist or is insignificant, inverting the observations from presumably "normal" ocean floor to derive a global best-fit depth-age relationship. However, just as the amplitude of eustatic sea level fluctuations cannot be gleaned from any single locality (Bond, 1978), it is equally difficult to estimate the anomalous depth of oceanic basement at a given location. What the two problems have in common is the ubiquity of mantle-driven dynamic topography that affects the surface of the Earth at any given site

(Figs 2-4). It follows that an inversion for a depth-age curve from sediment-unloaded oceanic basement depths that is expected to solely reflect thermal boundary layer cooling and/or plate-model-related time-dependent small-scale convection beneath oceanic plates will inherit biases from any other process that is ignored. A review of published numerical dynamic topography models (Flament et al., 2013) illustrates that large parts of the ocean basins are particularly affected by positive dynamic topographic anomalies owing to large-scale upwellings – this can also be seen in the models used here (Figs 2-4). While considering that the amplitude of these topographic features is uncertain, this nevertheless suggests that this bias may lead to excess plate model flattening of old ocean floor, affecting the comparison of residual topography and numerically computed dynamic topography, if computed residual topography is based on a reference oceanic-depth age model that has inherited dynamic topography signals. Our spectral analysis of these models demonstrates that if the uncertainty in oceanic depth-age models is considered in this context, then the power spectra of models M5-M7 are too red only at degree 1 (Fig. 5), representing a significant improvement over previous models. At spherical harmonic degrees 2 and 3, the r.m.s. dynamic topography amplitude of model M7 is 740 m, and 570 m, respectively, within the range of residual topography end-members at 850 m (thermal boundary layer (TBL) subsidence only) and 530 m (plate model (PM) subsidence) at degree 2 and 770 m (TBL) and 510 m (PM) at degree 3. This suggests that at degree 2, Crosby and Mckenzie's (2009) plate subsidence model may be contaminated by about 200 m of deep mantle convection-driven dynamic topography. However, it needs to be kept in mind that our preferred model M7 still overestimates the amplitude of dynamic topography at spherical degree 1 as estimated by Hoggard et al. (2016) by at least 700 m, but the magnitude of residual topography at these long wavelengths is still debated (Yang and Gurnis, 2016). Discrepancies between residual topography and dynamically computed topography at long wavelengths possibly reflect the computation of dynamic topography from sources below 350 km depth, well below the depth of continental cratonic keels and below the depth to which slabs are assimilated in the models, as well as the inherent limitations in spherical harmonic expansion of a limited global point data set (Yang and Gurnis, 2016).

We find that our geodynamic forward model M7 provides the best overall fit to paleogeography-derived continental inundation (Fig. 14). All models generally match geological observations better for the last 60 million years than for earlier times. The mean Cenozoic differences between geodynamically-modelled versus geologically-reconstructed land fractions are within ±5% with the exception of M6, and the land fraction differences based on the two alternative paleogeography reconstructions are overall similar (Fig. 14). This reflects a consensus in the reconstructions of Cenozoic paleogeography and that our models match them well overall. African land fractions are nearly always underestimated with the exception of model hybrid model M1. Forward models that include plumes (M5 and M6) are less useful for modelling continental dynamic topography, as in these models plumes evolve fully dynamically such that neither the time nor the location of their initial arrival at the surface can be well tuned to match the observed occurrence of plume-related uplift. This emphasises the future prospects of models with sequential data assimilation. Model M7, in which plumes are suppressed and which is characterised by relatively moderate dynamic topography amplitudes as compared to models M1-4, overall fits the land fraction for all continents as compared with Golonka’s (2007) paleoshorelines, with the exception of the Late Cretaceous flooding of Africa (due to lacking plumes) (Fig. 14e). Using

Smith et al.'s (1994) paleoshorelines worsens the fit for Australia and Eurasia, with M7 underestimating continental flooding (Figs 14f, j).

It is important to note that agreement between modelled and inferred land fractions is possible even if the flooded regions only partially coincide spatially. Therefore it is essential to evaluate the model agreement in land fractions jointly with spatial overlaps (Fig. 14). Model M1 performs slightly better than other models for land fraction overlaps, with the best matches in Australia, Eurasia, Africa and North America, while South American paleogeography is less well matched, possibly because Andean flat slabs were not incorporated in Model M1. On the other hand, even though South American flat slabs are included in M2-M7, only M2 and M7 result in reasonable fits to geologically mapped South American inland seas for Golonka's (2009) Cenozoic paleogeography (Fig. 14c), while using Smith et al.'s (1994) paleo-coastlines improves the South American match for most models (Fig. 14h), suggesting that the latter paleogeography might be better constrained for the Cenozoic of South America than the former. By the same token the match in Australia is slightly improved for nearly all models using Smith et al.'s (1994) paleogeography, underlining its greater similarity to the detailed Australian paleogeography by Langford et al. (1995) in the Cenozoic as compared with Golonka's (2009). In contrast, using Golonka's (2009) paleogeography considerably improves the model match for North America as compared with Smith et al.'s (1994), highlighting that currently there is no single preferred global model for paleo-coastlines on all continents.

Model M7 maximises the combined inundation overlap for Eurasia, Africa, South and North America, but misfits the Cenozoic flooding of Australia (Fig. 14c, d). It has been shown before that the inclusion of a large mantle upwelling straddling East Antarctica is important for modelling Australia’s dynamic topography in the Cenozoic, as the continent progressively moved away from this upwelling and towards the dynamic low associated with Southeast Asian subduction zones (DiCaprio et al., 2011). In the models analysed here, the mantle structure associated with this upwelling is only considered in Model M1, and this explains why M1 outperforms all other models in terms of replicating Australia’s Cenozoic inundation patterns (Fig. 14c, d). Overall, modelled versus geologically reconstructed land fractions match within 10% for most models, and the spatial overlaps of inundated regions are mostly between 85% and 100% for the Cenozoic, dropping to about 75-100% in the Cretaceous.

In terms of dynamic topography of passive margins through time, the favoured model M7 results in up to 500 (±150) m of tectonic subsidence of continental interiors while along passive margins the maximum predicted dynamic topographic change over 140 million years is about 350 (±150) m of subsidence, substantially smaller than the total tectonic subsidence caused by rifting. Typical rates of dynamic topographic change range from +/-10m/Myr (Model M7, Figs 15, 16). In an extended Boussinesq model in which plumes are suppressed, such as M7, passive margins exhibit a more pronounced tendency to be affected by uplift than continental interiors, but the mean amplitude of this effect is only of the order of 100 ±50m, because dynamic topography amplitudes in all extended Boussinesq models are smaller overall compared with other models. Other models, such as M3, which shares the same plate model with M7, also perform reasonably well in terms of modelled land fractions and inundation overlaps, but we favour M7 because of its improved match to residual oceanic topography at long wavelengths. Models with plumes can result in more pronounced passive margin uplift of about 200 ±200m. This effect is more pronounced along continental margins than interiors because some passive margins have either moved over the periphery of a large mantle upwelling, like eastern Australia (Müller et al., 2016) or have been affected by a mantle plume through time, with the northeast coast of Brazil being a potential example (Mizusaki et al., 2002). Australia and South American are also the two continents exhibiting the largest long-term gradients in mean rates of change in dynamic topography (Fig. 16), with Australian experiencing growing rates of subsidence throughout the Cenozoic, reflecting its northeastward migration towards the Melanesian slab burial ground, while South America experiences a gradual increase in uplift rates over the last 40 million years, reflecting an intensification of the large-scale mantle upwelling centered on Africa, straddling the east coast of South America, paired with a rebound of the west coast of South America from being previously drawn down by the sinking Farallon slab (Fig 4).

Conclusions

We have carried out a global analysis of mantle convection-driven dynamic surface topography for the last 140 Ma, using seven geodynamic models combined with alternative eustatic sea level curves, and evaluated predicted continental flooding patterns against two alternative sets of geologically-derived paleo-coastlines. After evaluating the power spectra of the dynamic topography models, the match between model predictions and published paleo-coastlines is established based on computing modelled land fractions as well as inundation overlaps through time. We find that forward geodynamic model M7, which is based on an extended Boussinesq approximation and a mantle viscosity profile similar to that of Steinberger and Calderwood (2006), provides the best overall fit to geologically-derived continental inundation. Model M3 also performs fairly well, reflecting that M3 and M7 are based on the same recent plate model. However, for the last 60 million years, model

M1 fits best, reflecting a backward-forward modeling approach with an assimilated tomographically-imaged mantle structure into forward models that works well for the recent geological past. For the Cenozoic, model M1 also stands out by performing better than all other models for matching Africa's flooding history, both in terms of land fractions and inundation overlaps. Our model evaluation reveals that our overall best-fit model M7 fits Golonka's (2007, 2009) paleogeography somewhat better than Smith et al.'s (1994) in the Cretaceous, whereas the alternative paleo-coastline reconstructions are roughly equivalent in the Cenozoic, with the exception for Australia and South America, where modelled inundation is better matched by Smith et al.'s (1994) paleogeography.

We categorise the evolution of modelled dynamic topography in both continental interiors and along passive margins using cluster analysis to investigate how clusters of similar dynamic topography time series are distributed spatially. A subdivision of four clusters is found to best reveal end-members of dynamic topography evolution, differentiating topographic stability, long-term pronounced subsidence and initial stability over a dynamic high followed by moderate subsidence. The fourth cluster represents regions that are always proximal to subduction zones, and exhibits evolutionary paths including initial subsidence followed by uplift, or accelerating subsidence through time. This four-cluster categorisation of continental dynamic topography through time is mirrored by passive margins. The most commonly observed process is a gradual movement of passive margins from dynamic highs towards dynamic lows during the fragmentation of Pangea, reflecting that many continental passive margins now overlie slabs sinking in the lower mantle. This may explain why passive margin highlands are relatively rare.

The overall match between predicted dynamic topography, modulated by eustasy, to geologically mapped paleo-coastlines through time in terms of land fractions and inundation overlaps suggests that mantle-driven dynamic topography is a critical component of relative sea level change, and indeed the main basis for understanding the patterns of large-scale continental inundation through time. By ground-truthing models using the flooding history of continental interiors, we have established a robust method for evaluating dynamic topographic change along passive continental margins, where dynamic topography signals are more difficult to detect in the geological record.

Geodynamic forward models that are well calibrated for relatively recent geological periods in terms of their predicted dynamic topography open up the opportunity to model dynamic surface topography in the Early Mesozoic and Paleozoic, as plate models with topologically closing plate boundaries ranging from the Devonian Period to the present (e.g. Matthews et al., (2016) become available. This would lead to an improved understanding of large-scale continental uplift and subsidence and the interplay between shifting coastlines, sediment sources and sinks through time. Coupling this approach with surface process models (e.g. Salles and Hardiman, 2016) would provide a more quantitative understanding of the origin and pathways of sediments that have filled sedimentary basins through time, and would provide genetic insights into the stratigraphy of individual basins and margins.

Acknowledgments

This work was supported by Australian Research Council grants ARC grants DP130101946, IH130200012 and DE160101020, and by resources from the National Computational Infrastructure (NCI), which is supported by the Australian Government. MG was supported by the National Science Foundation (EAR ‐ 1247022, EAR- 1358646, and EAR- 1645775) and Statoil ASA. We thank Lauren Harrington for editing some figures and proofreading the manuscript. An interactive globe on the GPlates Portal (portal.gplates.org) will allow users to explore the detailed predictions of individual models presented here for any given continental and passive margin locations.

Figure Captions

Fig. 1. Alternative global sea level curves used in combination with modelled dynamic topography. The red- green- and blue-dotted curves show the sea level curves derived from the oceanic age-area distributions through time from Müller et al. (2016), Seton et al. (2012), and (Spasojevic and Gurnis, 2012), modified from Müller et al. (2008), respectively. The large difference in the amplitude of these curves reflects the uncertainty in reconstructing now subducted ocean floor, particularly in the Pacific and Tethys, including now destroyed Cretaceous Tethyan back-arc basins. The large drop in sea level back in time from 120 to 140 Ma visible in both curves is an artefact reflecting an underestimate in the length of the global mid-ocean ridge system at these times, especially in terms of back-arc basins, as well as our insufficient knowledge of oceanic plateaus before 120 Ma. The blue and black curves show the preferred sea level curves in Spasojevic and Gurnis (2012) and Haq et al. (1987), respectively. The red and green areas show the range of global sea level estimates obtained from combining ocean basin volume-derived sea level with oceanic

dynamic topography (DYN) from global convection models with the exception of model M1 which is based on a different modelling approach combining the effects of mean oceanic and continental dynamic topography on eustasy. Including dynamic topography effects enhances modelled sea level highs, because the majority of the ocean basins are dominated by large-scale mantle upwellings.

Fig. 2. Modelled dynamic topography in model M1 at 10 Myr intervals, with reconstructed continents (Gurnis et al., 2012) overlain.

Fig. 3. Modelled dynamic topography in model M3 at 10 Myr intervals, with reconstructed continents (Müller et al., 2016) overlain.

Fig. 4. Modelled dynamic topography in model M7 at 10 Myr intervals, with reconstructed continents (Müller et al., 2016) overlain.

Fig. 5. Power spectra of present-day dynamic topography for models M1-7. The spectra of residual depth anomalies calculated with the depth-age plate model of Crosby and McKenzie (2009) (light gray) and a half-space cooling model (dark gray) are taken from Hoggard et al. (2016). The scale of the power is given km^2; taking the square root of the power at a given degree will provide amplitude, as discussed in the text.

Fig. 6. Mean dynamic topography through time for each continental region considered here.

Fig. 7. Mean oceanic dynamic topography for models presented in this study through time. The long-term trend in the evolution of oceanic dynamic topography in models in group A (top) shows a sharp contrast with that from models in group B (bottom). This is a consequence of cold subducting slabs playing a more significant role in models M1-M4 (group A). In these models slabs do not heat up as they descend into the mantle and thus trigger a larger return flow as compared with models in which descending slabs do heat up. In models M1-M4 the evolution of dynamic topography therefore directly reflects the evolution of the age distribution, and thickness, of subducting oceanic lithosphere through

time, which directly controls the buoyancy of slabs. In contrast, in models M5-M7 cold subducting slabs undergo viscous heating as they descend into the mantle, and more importantly, models in this group include plume upwellings (although suppressed in model M7) that could reflect the long-term rise in cumulative large igneous province (LIP) volumes since 150 Ma (Yale and Carpenter, 1998), even though the process of melting and LIP generation is not included in our models. Hence oceanic dynamic topography in these models shows a steady increase towards present-day.

Fig. 8. (a (i)) The solid curve (DYN_{M1}-SG12) shows the sea level curve used in (Spasojevic and Gurnis, 2012) combining ocean-basin volume effects with the contribution of oceanic dynamic topography, while the dotted curve (SG12) shows the curve based on the oceanic age-area distribution from Müller et al. (2008), with the shaded region illustrating the contribution of oceanic dynamic topography. We show the effects of sea level curves with and without correction for mean oceanic dynamic topography in all our models, considering that sea level curves without this contribution represent an underestimate, but curves including oceanic dynamic topography may overestimate global sea level amplitudes, given that the geodynamic models overestimate dynamic topography amplitudes at long wavelengths (Fig. 5).

(a (ii)) The distribution of oceans and continents predicted in model M1, using the SG12 sea level curve based on (Müller et al., 2008), is shown in the first column at labelled ages (see methods for more details). The second column shows equivalent predictions based on the $\mathrm{DYN_{M1}}$-SG12 sea level curve. The distribution of oceans and continents in the paleogeography models of Smith et al. (1994) and Golonka (Golonka, 2007, 2009) are shown in the third and fourth columns, respectively.

(b) Evolution of the fraction of land, $\tau(t)$, over the last 90 Ma as predicted in model M1, based on sea level curves SG12 (blue) and $\mathrm{DYN_{M1}}$-SG12 (black) are shown on the first column for each labelled continent. Evolution of the fraction of land, $\tau(t)$, computed for paleogeography grids from Smith et al. (1994) and Golonka (2007, 2009) are also shown in red and green, respectively, for labelled ages in the first column. The yellow and black curves in the second column show the evolution of spatial overlap, $\mu(t)$, (see methods) between predictions of inundation patterns within each continent in model M1, based on sea level curve SG12, and those from paleogeography grids (Golonka, 2007, 2009; Smith et al., 1994). The cyan and magenta curves show the equivalent result, but for sea level curve $\mathrm{DYN}_{\mathrm{M1}}$-SG12.

Fig. 9. (a (i)) Same as in Fig. 6a(i) but for model M3 and is based on the sea level curve indicated – see Fig 1. for sea level keys. (a (ii)) Same as in Fig. 6a(ii), b (Golonka, 2007, 2009) but for model M3 and based on sea level curves as indicated. (b) Same as in Fig. 6b, but for model M3 and based on sea level curves as indicated, with the time ranging from 140 Ma to the present.

Fig. 10. (a (i)) Same as in Fig. 6a(i) but for model M7 and is based on the sea level curve indicated – see Fig 1. for sea level keys. (a (ii)) Same as in Fig. 6a(ii), b (Golonka, 2007, 2009) but for model M7 and based on sea level curves as indicated. (b) Same as in Fig. 6b, but for model M7.

Fig. 11. (a) Cluster analyses of modelled continental dynamic topography in model M1 over the last 90 Ma (see methods and Table 3). (b) Evolution of dynamic topography within each cluster, with $\pm1\sigma$ envelopes. (c) Same as in (a), but with analyses restricted to passive margin regions only. (d) Same as in (b), but for clusters shown in (c).

Fig. 12. (a) Cluster analyses of modelled continental dynamic topography in models M2-M7. (b) Evolution of dynamic topography within each cluster, with $\pm1\sigma$ envelopes.

Fig. 13. (a) Cluster analyses of modelled continental dynamic topography, restricted to passive margin regions only, in models M2-M7. (b) Evolution of dynamic topography within each cluster, with $\pm 1\sigma$ envelopes.

Fig. 14. Predictions shown here from models M1-M7 are based on their respective sea level curves, which include contributions from oceanic dynamic topography – see Figs 6-8 and Supp. Figs 8-11 for more details. (a) Deviations of mean fractions of land predicted by models M1-7 from that implied in paleogeography grids in Golonka (2007, 2009) for each continent, between 0 – 60 Ma, are shown in columns 1-5. Blue colours indicate overestimates of continental flooding, whereas red colours indicate excess land areas in our models. Hatched patterns for model M1 indicate absent model outputs in the Early Cretaceous, as this model only spans the time period from 0-90 Ma. The last column shows r.m.s. deviations for all continents over the same period as an indicator of the overall global model-data match for a given time period. (b) Same as in (a), but using paleogeography grids in Smith et al. (2007, 2009). (c) Mean spatial overlaps between predictions of inundation patterns within each continent in models M1-7 and those implied in paleogeography grids in Golonka (1994), between 0 – 60 Ma are shown in columns 1-5. Warm colours indicate larger spatial overlap than cool colours. The last column shows the mean spatial overlap for all continents over the same period. (d) Same as in (c), but using paleogeography grids in Smith et al. (1994). (e-h) Same as in (a-d), but for the time interval between 60 – 100 Ma. (i-l) Same as in (a-d), but for the time interval between 100 – 140 Ma.

Fig. 15. Rates of change of dynamic topography from our preferred model M7 in 10 million year intervals from 140 Ma to the present. Blue colours indicate subsidence while red colours indicate uplift.

Fig. 16. Mean rates of change of dynamic topography and standard deviations for individual continental regions considered here.

Parameter	Symbol	Value (Model M1)	Value (Models M2-4)	Value (Models M5-7)	Units
Rayleigh Number	Ra	7.5×10^{7}	7.8×10^{7}	5×10^{8}	
Thermal expansion coefficient	α_0	3×10^{-5}	3×10^{-5}	1.42×10^{-5}	K^{-1}
Density	ρ_0	3340	4000	3930	kg m^{-3}
Gravity acceleration	g_0	9.81	9.81	10	m s^{-2}
Temperature change	ΔT	2800	2825	3500	K
Mantle thickness	h_M	2867	2867	2867	km
Thermal diffusivity	κ_0	1×10^{-6}	1×10^{-6}	1×10^{-6}	m^2 s^{-1}
Viscosity	η_0	1×10^{21}	1×10^{21}	1×10^{21}	Pa s
Activation energy	E_η	348, upper mantle 348, lower mantle	100, upper mantle 33, lower mantle	233, upper mantle 320, lower mantle	kJ mol^{-1}
Activation Volume[a]	V_η	N/A	N/A	1.5×10^{-6}, upper mantle 6.7×10^{-6}, lower mantle	m^3 mol^{-1}
Temperature offset	T_η	1400	452	560	K
Dissipation Number[b]	Di	N/A	N/A	0.8	
Background mantle temperature[c]	T_b	1400	1685	Depth-dependent	K
Radius of the Earth	R_0	6371	6371	6371	km

Table 1: *Parameters common to all model cases. Subscript "0" denotes reference values. Common parameter values between models in groups A and B are only shown for group A.*

[a] *Viscosity parameterization in group A models do not require the activation volume parameter.*

[b] *Only group B models employ the extended Boussinesq approximation and thus require a dissipation number.*

[c] *Background mantle temperature varies with depth in group B models.*

Name/Acronym	Plate Model	Viscosity profile	Additional notes
Model 1	Gurnis et al. (2012)	100,0.1,1,60	Combined backward/forward convection model, Spasojevic and Gurnis (2012) Model M2
Model 2	Seton et al. (2012)	1,0.1,1,100	Müller et al. (2016) Model 3
Model 3	Müller et al. (2016)	1,0.1,1,100	Müller et al. (2016) Model 2
Model 4	Van Der Meer et al. (2010)	1,0.1,1,100	(Flament et al., 2017) Model "Case 24"
Model 5	Seton et al. (2012)	0.05, 0.0001, 0.0025, 0.07	Model with plumes, Hassan et al. (2015) Model M3
Model 6	Müller et al. (2016)	0.05, 0.0001, 0.0025, 0.07	With plumes, (Barnett‐Moore et al., 2017), Model "Case C1"
Model7	Müller et al. (2016)	0.05, 0.0001, 0.0025, 0.07	As Model 6, but with plumes suppressed

***Table 2:** Tectonic boundary conditions and depth-dependence of viscosity of the models referred to in this study. For models M2-7, the viscosity profile is given by applying a factor to the reference model viscosity (1 x 10^{21} Pa s) above 160 km depth (lithosphere), between 160 and 310 km depth (asthenosphere), between 310 and 670 km depth (upper mantle) and below 670 km depth (lower mantle) in order to obtain depth-dependent viscosity in addition to temperature-dependent viscosity. For models M2-M7 these values represent the pre-exponential parameter, A, at four depths through the mantle (2007, 2009) for details.*

Model type	Cluster 1	Cluster 2	Cluster 3	Cluster 4
Model M1 (hybrid backward advection – forward model)	Long-term stability over dynamic high	Slow long-term subsidence over pronounced dynamic low	Slow long-term subsidence over low-amplitude dynamic low	
Geodynamic forward model group A (models M2-4)	Pronounced long-term subsidence	Stability with slow long-term uplift	Initial Early Cretaceous stability followed by gradually accelerating subsidence	Subsidence for most of the Cretaceous (140-80 Ma) followed by uplift
Geodynamic forward model group B (models M5-7)	Pronounced long-term subsidence	Slow long-term subsidence	Long-term stability over dynamic high with variable combinations of initial or late uplift/subsidence	Long-term slow subsidence over dynamic low

Table 3. *Cluster categories for alternative groups of geodynamic models using 4 clusters*

References

Allen, P.A., Allen, J.R., 2013. Basin analysis: Principles and application to petroleum play assessment. John Wiley & Sons.

Austermann, J., Mitrovica, J., 2015. Calculating gravitationally self-consistent sea level changes driven by dynamic topography. Geophysical Journal International 203, 1909-1922.

Barnett‐Moore, N., Hassan, R., Müller, R.D., Williams, S.E., Flament, N., 2017. Dynamic topography and eustasy controlled the paleogeographic evolution of northern Africa since the mid Cretaceous. Tectonics in review.

Bocher, M., Coltice, N., Fournier, A., Tackley, P., 2016. A sequential data assimilation approach for the joint reconstruction of mantle convection and surface tectonics. Geophysical Journal International 204, 200-214.

Bond, G., 1978. Speculations on real sea-level changes and vertical motions of continents at selected times in the Cretaceous and Tertiary periods. Geology 6, 247-250.

Bower, D.J., Gurnis, M., Flament, N., 2015. Assimilating lithosphere and slab history in 4-D Earth models. Physics of the Earth and Planetary Interiors 238, 8-22.

Braun, J., 2010. The many surface expressions of mantle dynamics. Nature Geoscience 3, 825-833.

Christensen, U.R., Yuen, D.A., 1985. Layered convection induced by phase transitions. Journal of Geophysical Research: Solid Earth 90, 10291-10300.

Cloetingh, S., 1988. Intraplate stresses: a new element in basin analysis, New perspectives in basin analysis. Springer, pp. 205-230.

Colli, L., Bunge, H.P., Schuberth, B.S., 2015. On retrodictions of global mantle flow with assimilated surface velocities. Geophysical Research Letters 42, 8341-8348.

Colli, L., Ghelichkhan, S., Bunge, H.P., 2016. On the ratio of dynamic topography and gravity anomalies in a dynamic Earth. Geophysical Research Letters.

Colli, L., Stotz, I., Bunge, H.P., Smethurst, M., Clark, S., Iaffaldano, G., Tassara, A., Guillocheau, F., Bianchi, M.C., 2014. Rapid South Atlantic spreading changes and coeval vertical motion in surrounding continents: Evidence for temporal changes of pressure‐driven upper mantle flow. Tectonics 33, 1304-1321.

Conrad, C.P., Husson, L., 2009. Influence of dynamic topography on sea level and its rate of change. Lithosphere 1, 110-120.

Crosby, A.G., McKenzie, D., 2009. An analysis of young ocean depth, gravity and global residual topography. Geophysical Journal International 178, 1198-1219.

Czarnota, K., Roberts, G., White, N., Fishwick, S., 2014. Spatial and temporal patterns of Australian dynamic topography from River Profile Modeling. Journal of Geophysical Research: Solid Earth 119, 1384-1424.

De Grave, J., Buslov, M.M., 2007. Distant effects of India–Eurasia convergence and Mesozoic intracontinental deformation in Central Asia: constraints from apatite fission-track thermochronology. Journal of Asian Earth Sciences 29, 188-204.

DiCaprio, L., Gurnis, M., Müller, R.D., Tan, E., 2011. Mantle dynamics of continentwide Cenozoic subsidence and tilting of Australia. Lithosphere 3, 311-316.

DiCaprio, L., Müller, R.D., Gurnis, M., 2010. A dynamic process for drowning carbonate reefs on the northeastern Australian margin. Geology 38, 11-14.

English, J.M., Johnston, S.T., Wang, K., 2003. Thermal modelling of the Laramide orogeny: testing the flat-slab subduction hypothesis. Earth and Planetary Science Letters 214, 619-632.

Flament, N., Gurnis, M., Müller, R.D., 2013. A review of observations and models of dynamic topography. Lithosphere 5, 189-210.

Flament, N., Gurnis, M., Müller, R.D., Bower, D.J., Husson, L., 2015. Influence of subduction history on South American topography. Earth and Planetary Science Letters 430, 9-18.

Flament, N., Gurnis, M., Williams, S., Seton, M., Skogseid, J., Heine, C., Dietmar Müller, R., 2014. Topographic asymmetry of the South Atlantic from global models of mantle flow and lithospheric stretching. Earth and Planetary Science Letters 387, 107-119.

Flament, N., Williams, S., Müller, R., Gurnis, M., Bower, D., 2017. Origin and evolution of the deep thermochemical structure beneath Eurasia. Nature Communications 8, 14164.

French, S.W., Romanowicz, B., 2015. Broad plumes rooted at the base of the Earth's mantle beneath major hotspots. Nature 525, 95-99.

Golonka, J., 2007. Phanerozoic paleoenvironment and paleolithofacies maps: Mesozoic. Geologia/Akademia Górniczo-Hutnicza im. Stanisława Staszica w Krakowie 33, 211-264.

Golonka, J., 2009. Phanerozoic paleoenvironment and paleolithofacies maps: Cenozoic. Geologia/Akademia Górniczo-Hutnicza im. Stanisława Staszica w Krakowie 35, 507-587.

Gorski, K.M., Hivon, E., Banday, A., Wandelt, B.D., Hansen, F.K., Reinecke, M., Bartelmann, M., 2005. HEALPix: a framework for high-resolution discretization and fast analysis of data distributed on the sphere. The Astrophysical Journal 622, 759.

Guerri, M., Cammarano, F., Tackley, P.J., 2016. Modelling Earth’s surface topography: Decomposition of the static and dynamic components. Physics of the Earth and Planetary Interiors 261, 172-186.

Gurnis, M., 1993. Phanerozoic marine inundation of continents driven by dynamic topography above subducting slabs. Nature 364, 589-593.

Gurnis, M., Turner, M., Zahirovic, S., DiCaprio, L., Spasojevic, S., Muller, R., Boyden, J., Seton, M., Manea, V., Bower, D., 2012. Plate tectonic reconstructions with continuously closing plates. Computers and Geosciences 38, 35-42.

Haq, B.U., Hardenbol, J., Vail, P.R., 1987. Chronology of fluctuating sea levels since the Triassic. Science 235, 1156-1167.

Hassan, R., Flament, N., Gurnis, M., Bower, D.J., Müller, D., 2015. Provenance of plumes in global convection models. Geochemistry, Geophysics, Geosystems 16, 1465-1489.

Heine, C., Yeo, L., Müller, R., 2015. Evaluating global paleoshoreline models for the Cretaceous and Cenozoic. Australian Journal of Earth Sciences 62, 275-287.

Hoggard, M., White, N., Al-Attar, D., 2016. Global dynamic topography observations reveal limited influence of large-scale mantle flow. Nature Geoscience 9, 456-463.

Ita, J., King, S.D., 1994. Sensitivity of convection with an endothermic phase change to the form of governing equations, initial conditions, boundary conditions, and equation of state. Journal of Geophysical Research: Solid Earth 99, 15919-15938.

Japsen, P., Chalmers, J.A., Green, P.F., Bonow, J.M., 2012. Elevated, passive continental margins: Not rift shoulders, but expressions of episodic, post-rift burial and exhumation. Global and Planetary Change 90, 73-86.

Johan, H., Kleinspehn, K.L., 2000. Quantifying the timing and sense of fault dip slip: new application of biostratigraphy and geohistory analysis. Geology 28, 471-474.

Karato, S.-i., Wu, P., 1993. Rheology of the upper mantle: A synthesis. Science 260, 771-778.

Kirschner, J.P., Kominz, M.A., Mwakanyamale, K.E., 2010. Quantifying extension of passive margins: Implications for sea level change. Tectonics 29.

Langford, R.P., Wilford, G.E., Truswell, E.M., Totterdell, J.M., Yeung, M., Isem, A.R., Yeates, A.N., Bradshaw, M., Brakel, A.T., Olissoff, S., Cook, P.J., Strusz, D.L., 1995.

Palaeogeographic atlas of Australia: time dependent summarisation of sedimentological data based on several datasets, between 550 Ma to present day, In: Geoscience-Australia (Ed.), Canberra.

Larsen, T.B., Yuen, D.A., Malevsky, A.V., 1995. Dynamical consequences on fast subducting slabs from a self‐regulating mechanism due to viscous heating in variable viscosity convection. Geophysical Research Letters 22, 1277-1280.

Li, D., Gurnis, M., and Stadler, G., 2017, Towards adjoint-based inversion of time-dependent mantle convection with non-linear viscosity, Geophysical Journal International, 209, 86–105, doi: 10.1093/gji/ggw493.

Liu, L., Gurnis, M., 2008. Simultaneous inversion of mantle properties and initial conditions using an adjoint of mantle convection. Journal of Geophysical Research: Solid Earth 113.

Liu, S., Nummedal, D., Gurnis, M., 2014. Dynamic versus flexural controls of Late Cretaceous Western Interior Basin, USA. Earth and Planetary Science Letters 389, 221-229.

Lloyd, S., 1982. Least squares quantization in PCM. IEEE transactions on information theory 28, 129-137.

Lowell, J.D., 1995. Mechanics of basin inversion from worldwide examples. Geological Society, London, Special Publications 88, 39-57.

Matthews, K.J., Maloney, K.T., Zahirovic, S., Williams, S.E., Seton, M., Müller, R.D., 2016. Global plate boundary evolution and kinematics since the late Paleozoic. Global and Planetary Change 146, 226-250.

Maurer, F., Van Buchem, F.S., Eberli, G.P., Pierson, B.J., Raven, M.J., Larsen, P.H., Al‐Husseini, M.I., Vincent, B., 2013. Late Aptian long‐lived glacio‐eustatic lowstand recorded on the Arabian Plate. Terra Nova 25, 87-94.

Mizusaki, A.M.P., Thomaz-Filho, A., Milani, E.J., De Césero, P., 2002. Mesozoic and Cenozoic igneous activity and its tectonic control in northeastern Brazil. Journal of South American Earth Sciences 15, 183-198.

Moucha, R., Forte, A.M., Mitrovica, J.X., Rowley, D.B., Quéré, S., Simmons, N.A., Grand, S.P., 2008. Dynamic topography and long-term sea-level variations: There is no such thing as a stable continental platform. Earth and Planetary Science Letters 271, 101-108.

Müller, R.D., Flament, N., Matthews, K.J., Williams, S.E., Gurnis, M., 2016. Formation of Australian continental margin highlands driven by plate–mantle interaction. Earth and Planetary Science Letters 441, 60-70.

Müller, R.D., Sdrolias, M., Gaina, C., Steinberger, B., Heine, C., 2008. Long-term sea-level fluctuations driven by ocean basin dynamics. Science 319, 1357-1362.

Müller, R.D., Seton, M., Zahirovic, S., Williams, S.E., Matthews, K.J., Wright, N.M., Shephard, G., Maloney, K.T., Barnett-Moore, N., Hosseinpour, M., Bower, D.J., Cannon, J., 2016. Ocean basin evolution and global-scale plate reorganization events since Pangea breakup. Annual Review of Earth and Planetary Sciences 44, 107-138.

Pedersen, V.K., Huismans, R.S., Moucha, R., 2016. Isostatic and dynamic support of high topography on a North Atlantic passive margin. Earth and Planetary Science Letters 446, 1-9.

Ritsema, J., van Heijst, H.-J., Woodhouse, J.H., 2004. Global transition zone tomography. Journal of Geophysical Research 109, 10.1029/2003JB002610.

Roberts, G.G., White, N., 2010. Estimating uplift rate histories from river profiles using African examples. Journal of Geophysical Research: Solid Earth 115.

Rowley, D.B., Forte, A.M., Moucha, R., Mitrovica, J.X., Simmons, N.A., Grand, S.P., 2013. Dynamic topography change of the eastern United States since 3 million years ago. Science 340, 1560-1563.

Salles, T., Hardiman, L., 2016. Badlands: An open-source, flexible and parallel framework to study landscape dynamics. Computers & Geosciences 91, 77-89.

Sawyer, D.S., 1985. Total tectonic subsidence: a parameter for distinguishing crust type at the US Atlantic continental margin. Journal of Geophysical Research: Solid Earth 90, 7751-7769.

Schiffer, C., Nielsen, S.B., 2016. Implications for anomalous mantle pressure and dynamic topography from lithospheric stress patterns in the North Atlantic Realm. Journal of Geodynamics 98, 53-69.

Seton, M., Muller, R.D., Zahirovic, S., Gaina, C., Torsvik, T.H., Shephard, G., Talsma, A., Gurnis, M., Turner, M., Maus, S., Chandler, M.T., 2012. Global continental and ocean basin reconstructions since 200 Ma. Earth Science Reviews 113, 212-270.

Shephard, G.E., Flament, N., Williams, S., Seton, M., Gurnis, M., Müller, R.D., 2014. Circum‐Arctic mantle structure and long‐wavelength topography since the Jurassic. Journal of Geophysical Research: Solid Earth 119, 7889-7908.

Smith, A.G., Smith, D.G., Funnell, B.M., 1994. Atlas of Mesozoic and Cenozoic Coastlines. Cambridge University Press, Cambridge.

Spasojevic, S., Gurnis, M., 2012. Sea level and vertical motion of continents from dynamic earth models since the Late Cretaceous. AAPG bulletin 96, 2037-2064.

Spasojevic, S., Liu, L., Gurnis, M., Müller, R.D., 2008. The case for dynamic subsidence of the US east coast since the Eocene. Geophysical Research Letters 35, 8305-8305.

Stap, L.B., van de Wal, R.S.W., de Boer, B., Bintanja, R., Lourens, L.J., 2016. The influence of ice sheets on the climate during the past 38 million years. Clim. Past Discuss. in review.

Stein, C.A., Stein, S., 2015. Are large oceanic depth anomalies caused by thermal perturbations? Geological Society of America Special Papers 514, SPE514-512.

Steinberger, B., 2016. Topography caused by mantle density variations: observation-based estimates and models derived from tomography and lithosphere thickness. Geophysical Journal International 205, 604-621.

Steinberger, B., Calderwood, A.R., 2006. Models of large-scale viscous flow in the Earth's mantle with constraints from mineral physics and surface observations. Geophysical Journal International 167, 1461-1481.

Tackley, P.J., 1996. Effects of strongly variable viscosity on three‐dimensional compressible convection in planetary mantles. Journal of Geophysical Research: Solid Earth 101, 3311-3332.

Thoraval, C., Richards, M.A., 1997. The geoid constraint in global geodynamics: viscosity structure, mantle heterogeneity models and boundary conditions. Geophysical Journal International 131, 1-8.

Tosi, N., Yuen, D.A., de Koker, N., Wentzcovitch, R.M., 2013. Mantle dynamics with pressure-and temperature-dependent thermal expansivity and conductivity. Physics of the Earth and Planetary Interiors 217, 48-58.

Van Der Meer, D.G., Spakman, W., Van Hinsbergen, D.J., Amaru, M.L., Torsvik, T.H., 2010. Towards absolute plate motions constrained by lower-mantle slab remnants. Nature Geoscience 3, 36-40.

Xie, X., Müller, R.D., Li, S., Gong, Z., Steinberger, B., 2006. Origin of anomalous subsidence along the northern South China Sea Margin and its relationship to dynamic topography. Marine and Petroleum Geology 7, 745-765.

Yale, L.B., Carpenter, S.J., 1998. Large igneous provinces and giant dike swarms: proxies for supercontinent cyclicity and mantle convection. Earth and Planetary Science Letters 163, 109-122.

Yamato, P., Husson, L., Becker, T.W., Pedoja, K., 2013. Passive margins getting squeezed in the mantle convection vice. Tectonics 32, 1559-1570.

Yang, T., Gurnis, M., 2016. Dynamic topography, gravity and the role of lateral viscosity variations from inversion of global mantle flow. Geophysical Journal International 207, 1186-1202, doi: 10.1093/gji/ggw335.

Zahirovic, S., Flament, N., Müller, R.D., Seton, M., Gurnis, M., 2016. Large fluctuations of shallow seas in low‐lying Southeast Asia driven by mantle flow. Geochemistry, Geophysics, Geosystems 17, 3589–3607.

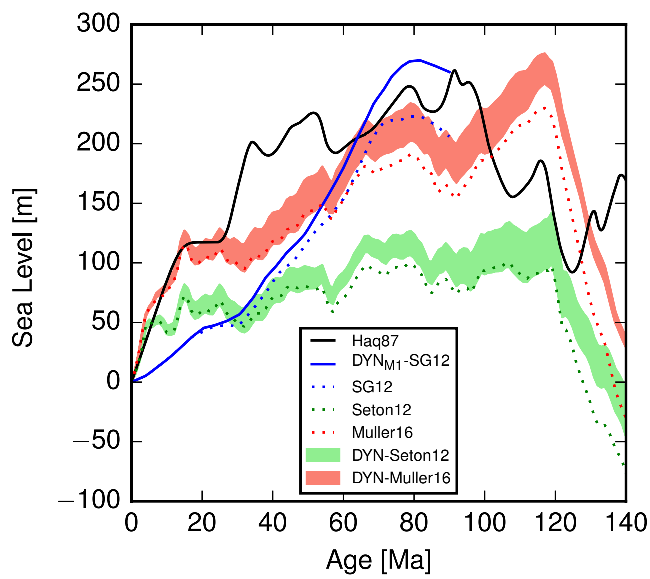

300
250
200
150
100
50
0
−50
−100
Sea Level [m]
0
20
40
60
80
100
120
140
Age [Ma]
Haq87
DYN$_{M1}$-SG12
SG12
Seton12
Muller16
DYN-Seton12
DYN-Muller16

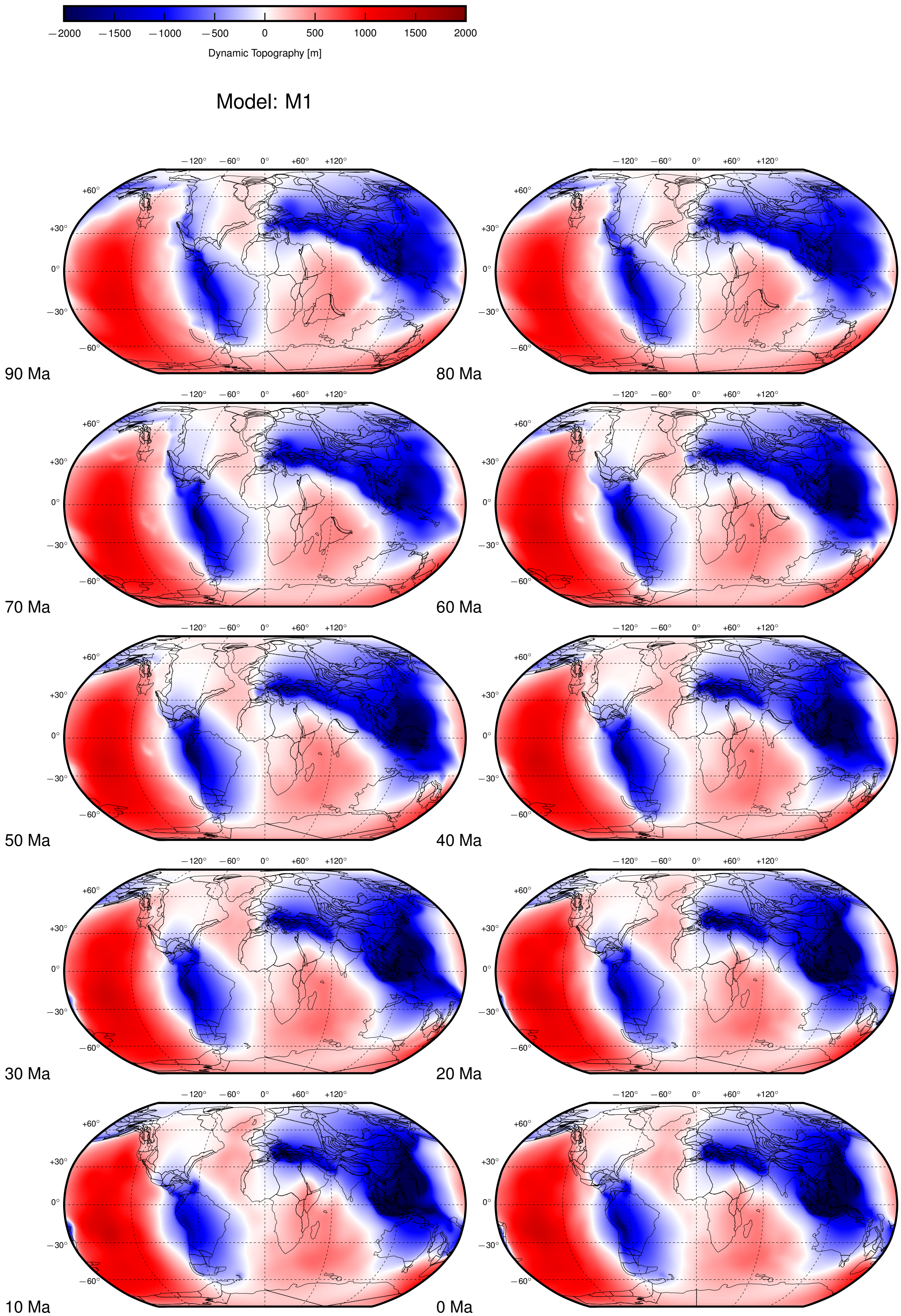

−2000 −1500 −1000 −500 0 500 1000 1500 2000
Dynamic Topography [m]
Model: M1
−120° −60° 0° +60° +120°
+60° +30° 0° −30° −60°
90 Ma
80 Ma
70 Ma
60 Ma
50 Ma
40 Ma
30 Ma
20 Ma
10 Ma
0 Ma

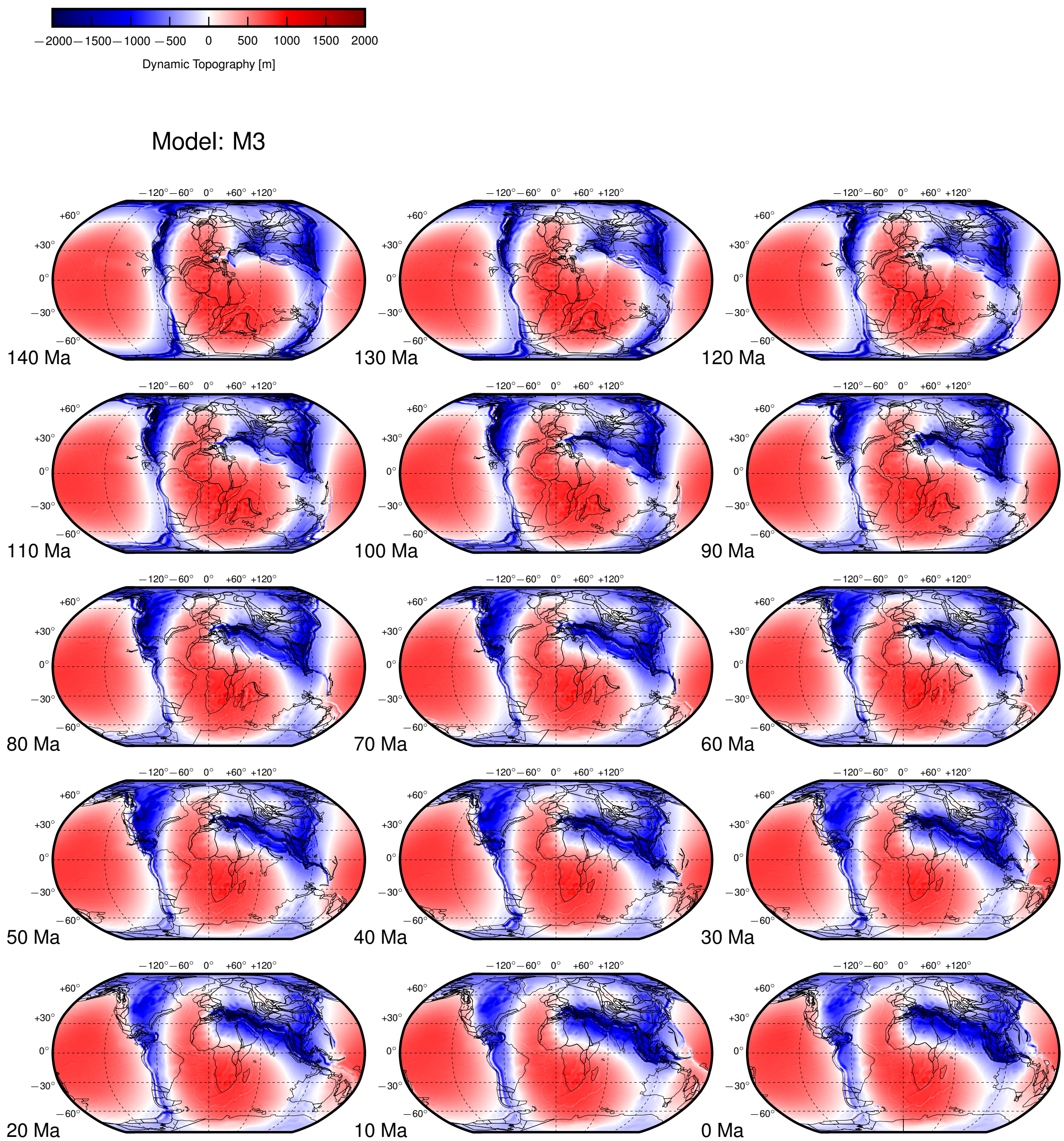

−2000 −1500 −1000 −500 0 500 1000 1500 2000
Dynamic Topography [m]
Model: M3
140 Ma
130 Ma
120 Ma
110 Ma
100 Ma
90 Ma
80 Ma
70 Ma
60 Ma
50 Ma
40 Ma
30 Ma
20 Ma
10 Ma
0 Ma

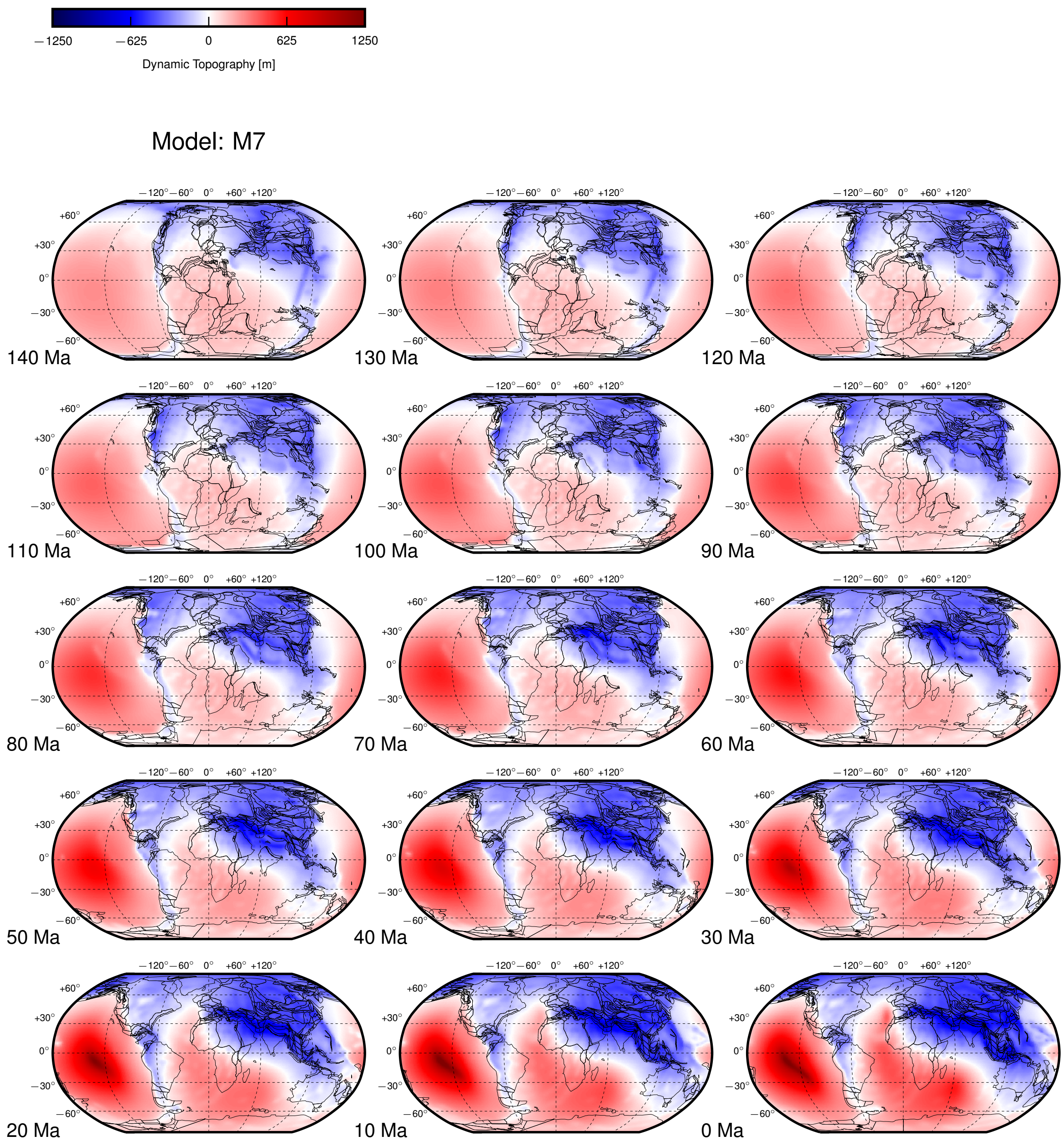

−1250
−625
0
625
1250
Dynamic Topography [m]
Model: M7
−120° −60° 0° +60° +120°
+60°
+30°
0°
−30°
−60°
140 Ma
130 Ma
120 Ma
110 Ma
100 Ma
90 Ma
80 Ma
70 Ma
60 Ma
50 Ma
40 Ma
30 Ma
20 Ma
10 Ma
0 Ma

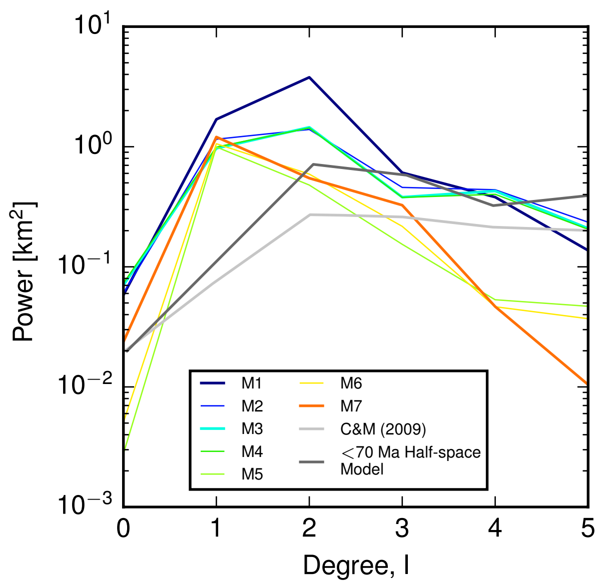

10^1
10^0
10^{-1}
10^{-2}
10^{-3}
Power [km^2]
0
1
2
3
4
5
Degree, l
M1
M2
M3
M4
M5
M6
M7
C&M (2009)
<70 Ma Half-space Model

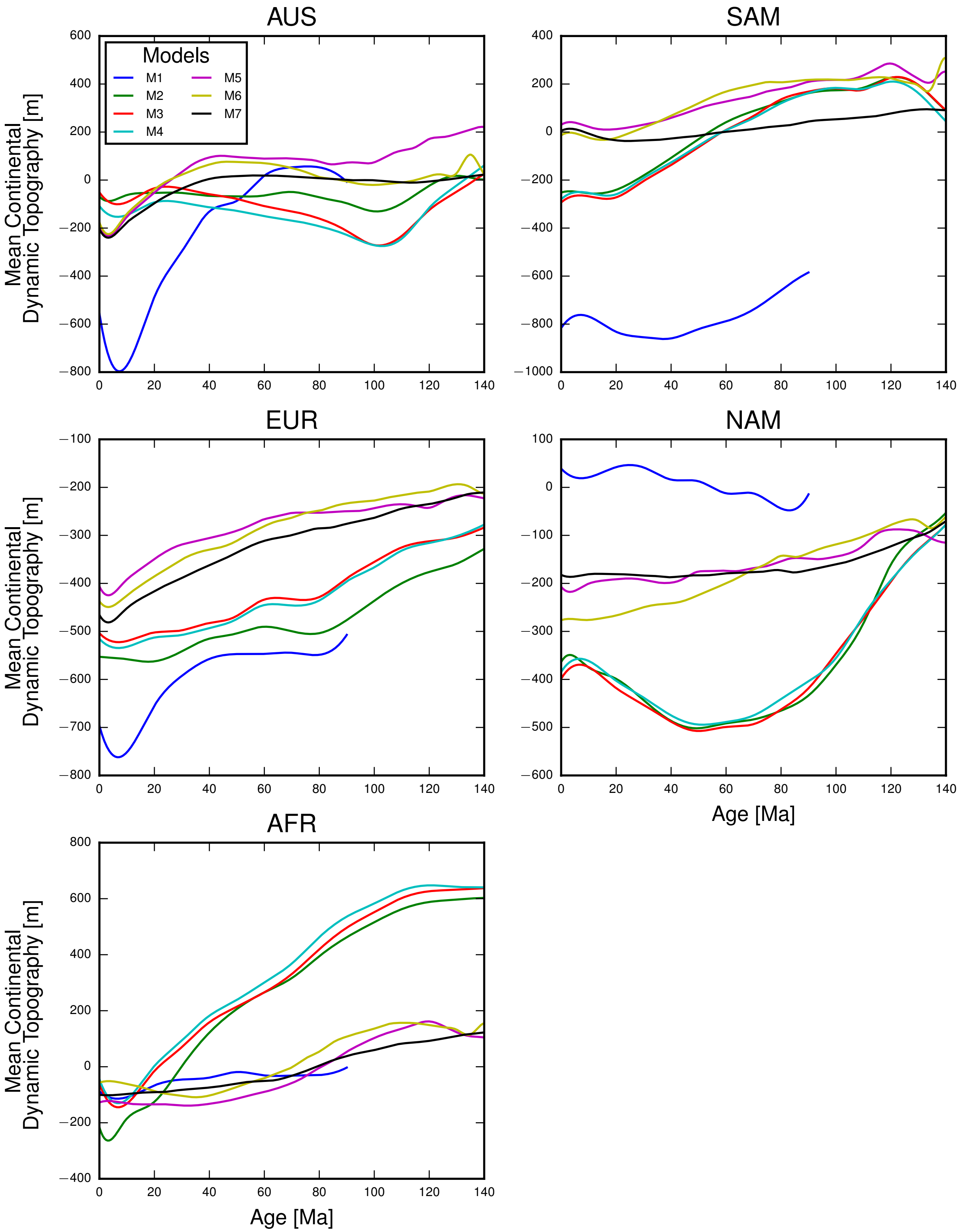
AUS
SAM
EUR
NAM
AFR
Models
M1
M2
M3
M4
M5
M6
M7
Mean Continental Dynamic Topography [m]
Age [Ma]

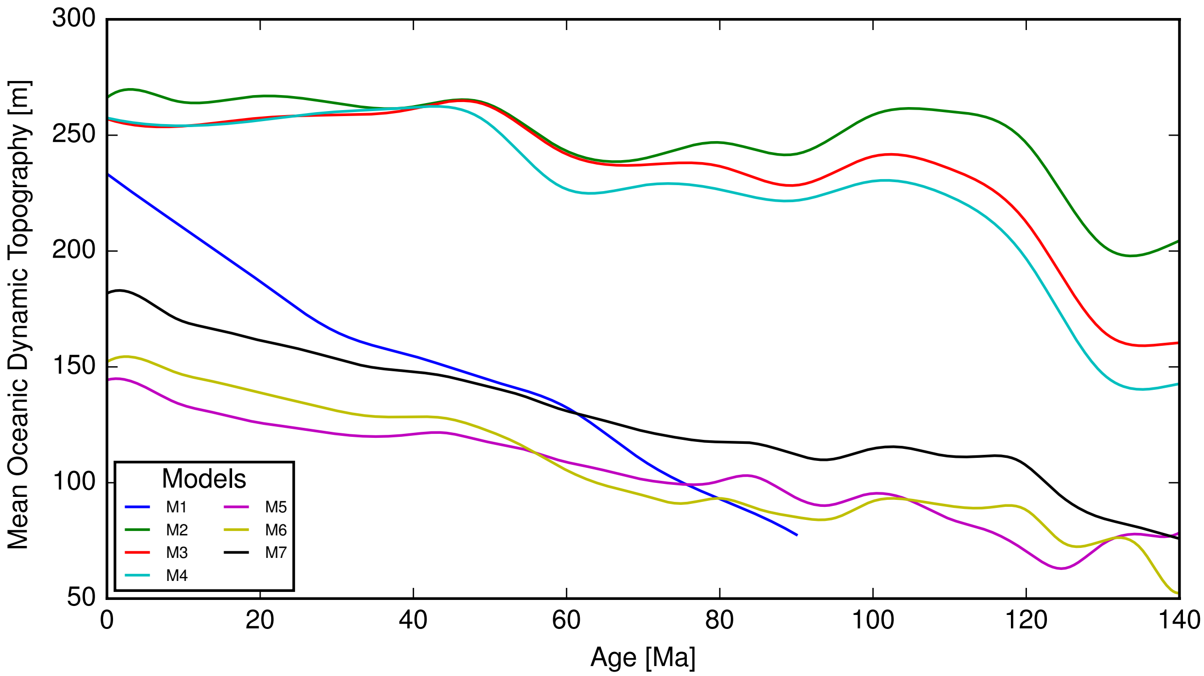

Mean Oceanic Dynamic Topography [m]
Age [Ma]
Models
M1
M2
M3
M4
M5
M6
M7
300
250
200
150
100
50
0
20
40
60
80
100
120
140

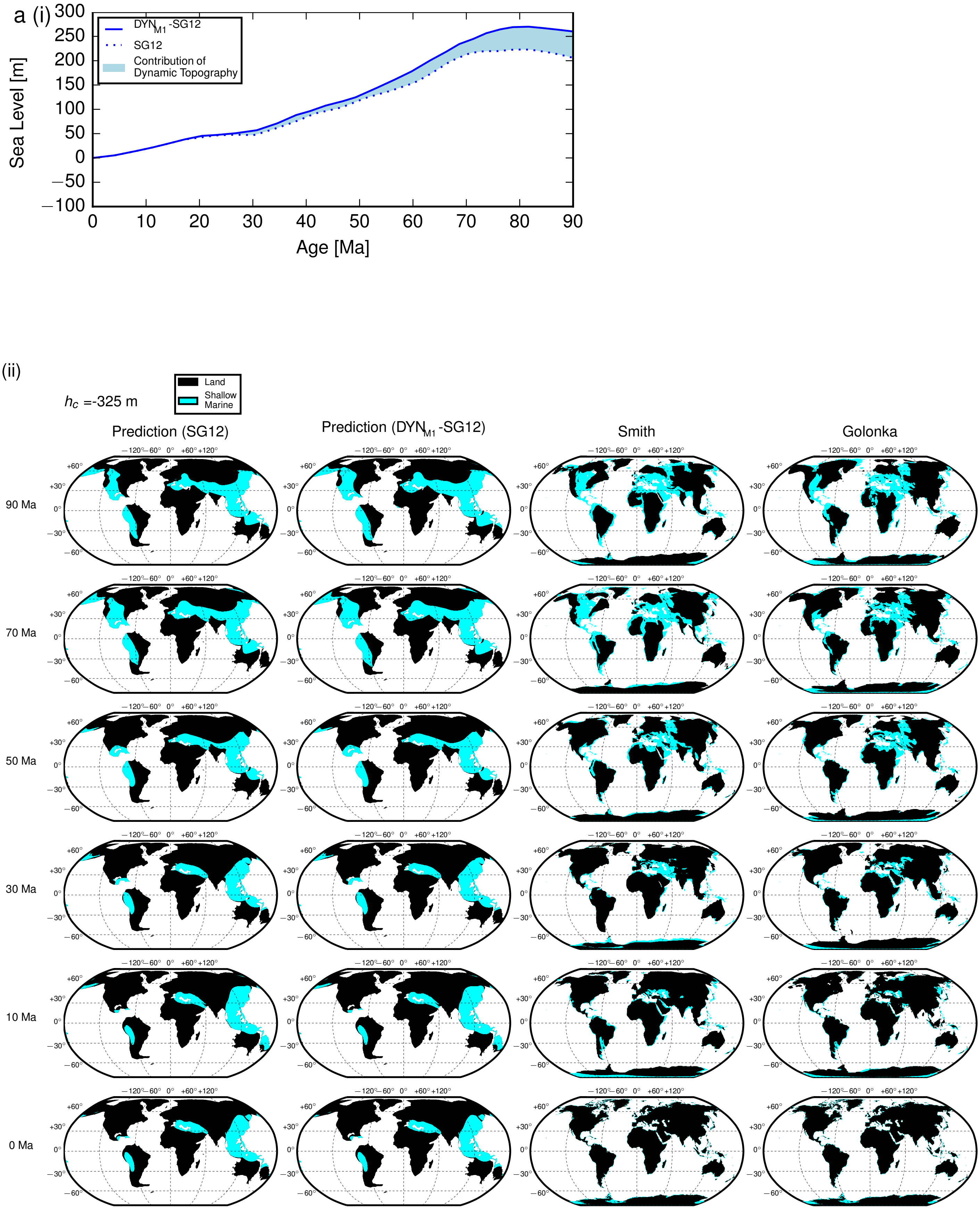

a (i)
Sea Level [m]
Age [Ma]
DYN$_{M1}$-SG12
SG12
Contribution of Dynamic Topography
(ii)
h_c =-325 m
Land
Shallow Marine
Prediction (SG12)
Prediction (DYN$_{M1}$-SG12)
Smith
Golonka
90 Ma
70 Ma
50 Ma
30 Ma
10 Ma
0 Ma

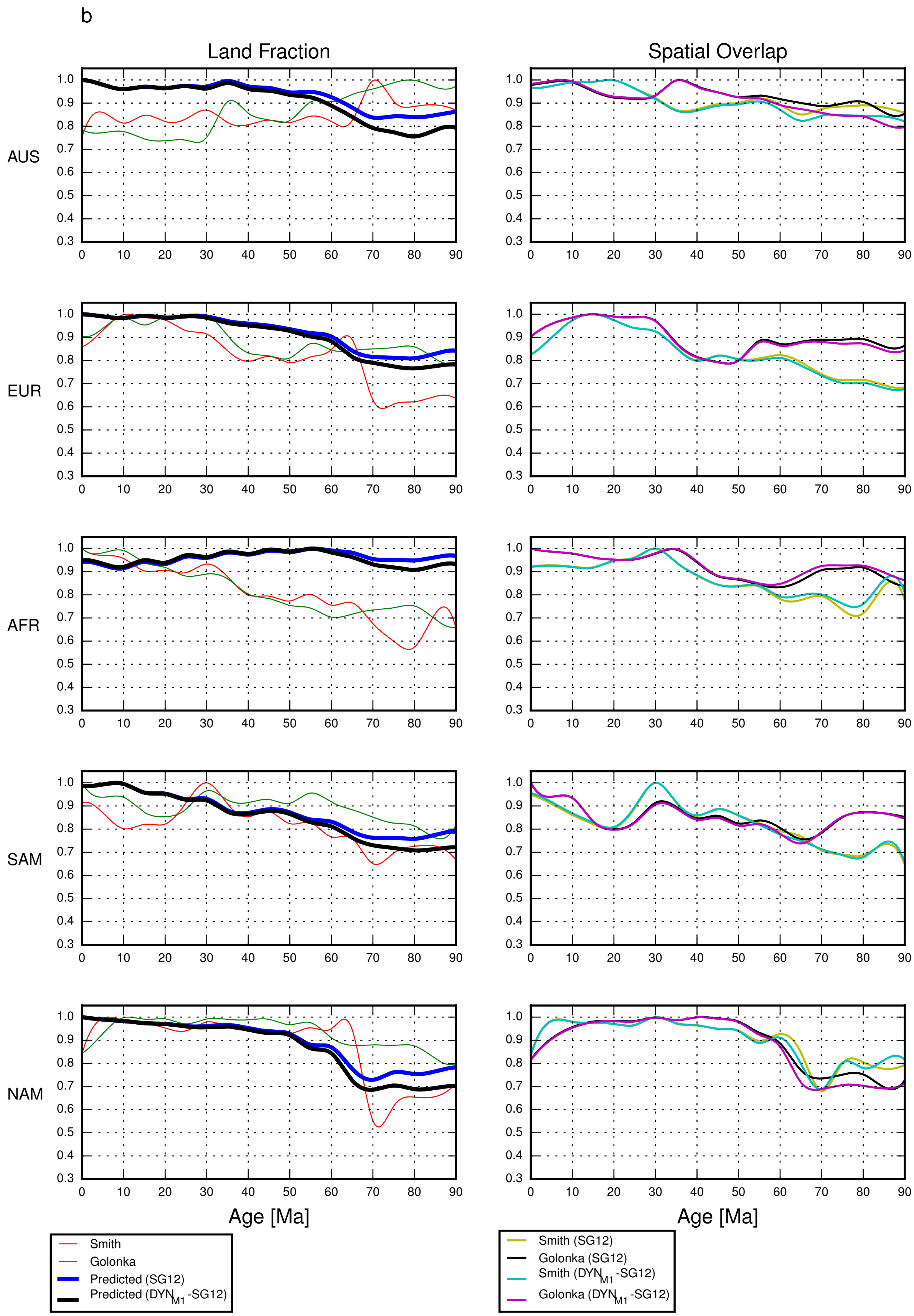
b
Land Fraction
Spatial Overlap
AUS
EUR
AFR
SAM
NAM
Age [Ma]
Age [Ma]
Smith
Golonka
Predicted (SG12)
Predicted (DYN$_{M1}$-SG12)
Smith (SG12)
Golonka (SG12)
Smith (DYN$_{M1}$-SG12)
Golonka (DYN$_{M1}$-SG12)

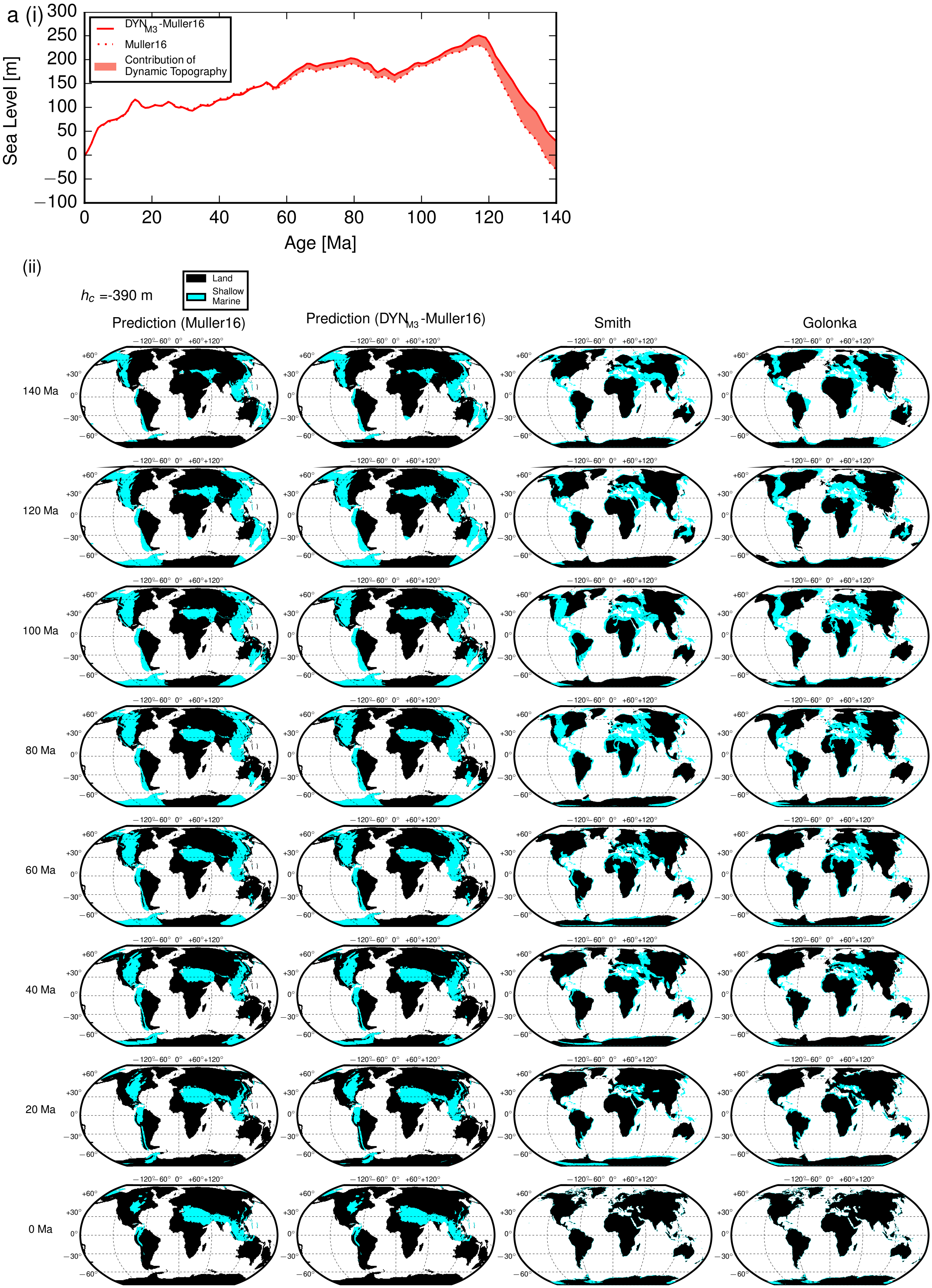
a (i)
DYN$_{M3}$-Muller16
Muller16
Contribution of Dynamic Topography
Sea Level [m]
Age [Ma]
300
250
200
150
100
50
0
−50
−100
0
20
40
60
80
100
120
140
(ii)
h_c =-390 m
Land
Shallow Marine
Prediction (Muller16)
Prediction (DYN$_{M3}$-Muller16)
Smith
Golonka
140 Ma
120 Ma
100 Ma
80 Ma
60 Ma
40 Ma
20 Ma
0 Ma
−120° −60° 0° +60° +120°
+60°
+30°
0°
−30°
−60°

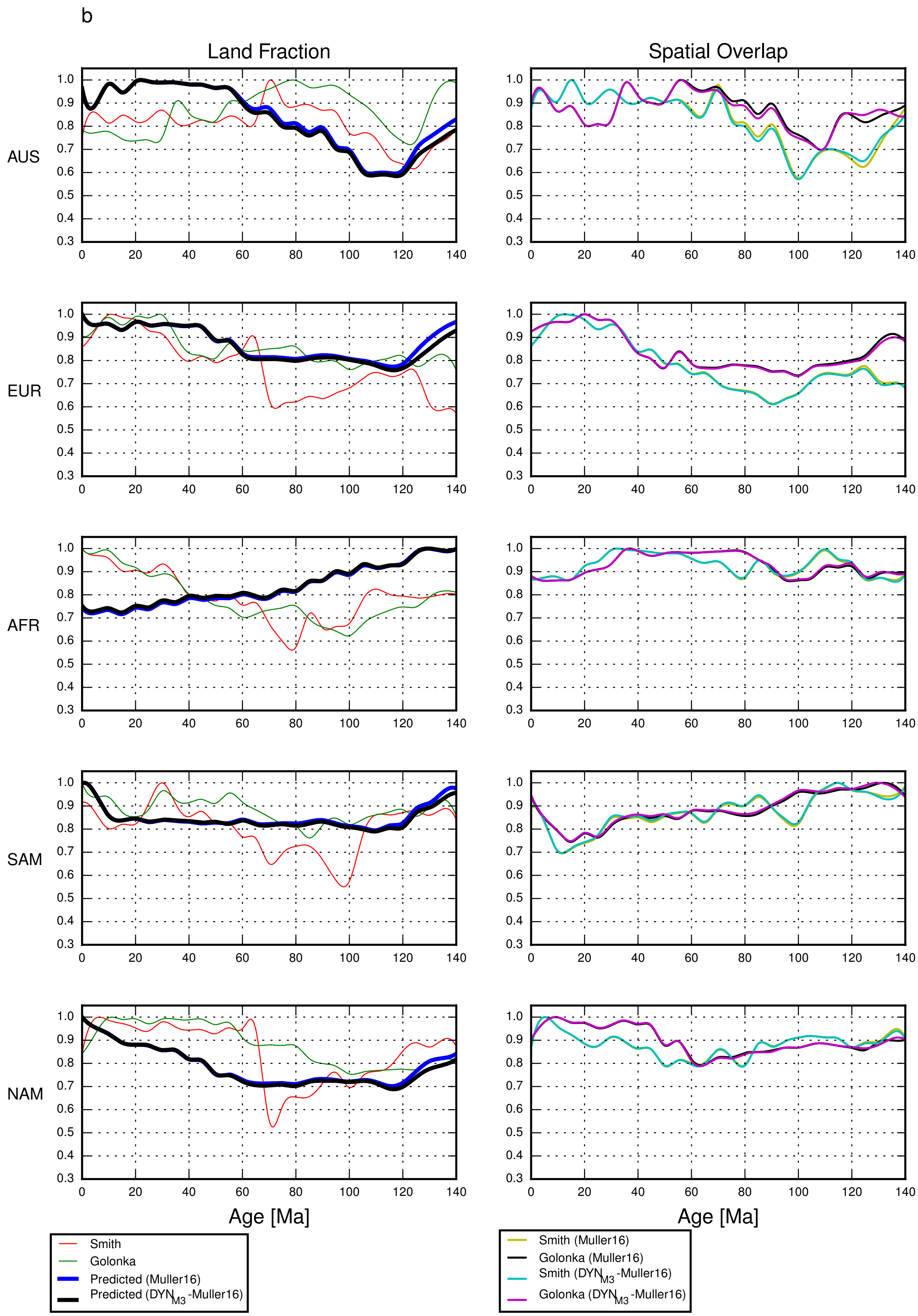

b
Land Fraction
Spatial Overlap
AUS
EUR
AFR
SAM
NAM
Age [Ma]
Age [Ma]
Smith
Golonka
Predicted (Muller16)
Predicted (DYN$_{M3}$-Muller16)
Smith (Muller16)
Golonka (Muller16)
Smith (DYN$_{M3}$-Muller16)
Golonka (DYN$_{M3}$-Muller16)

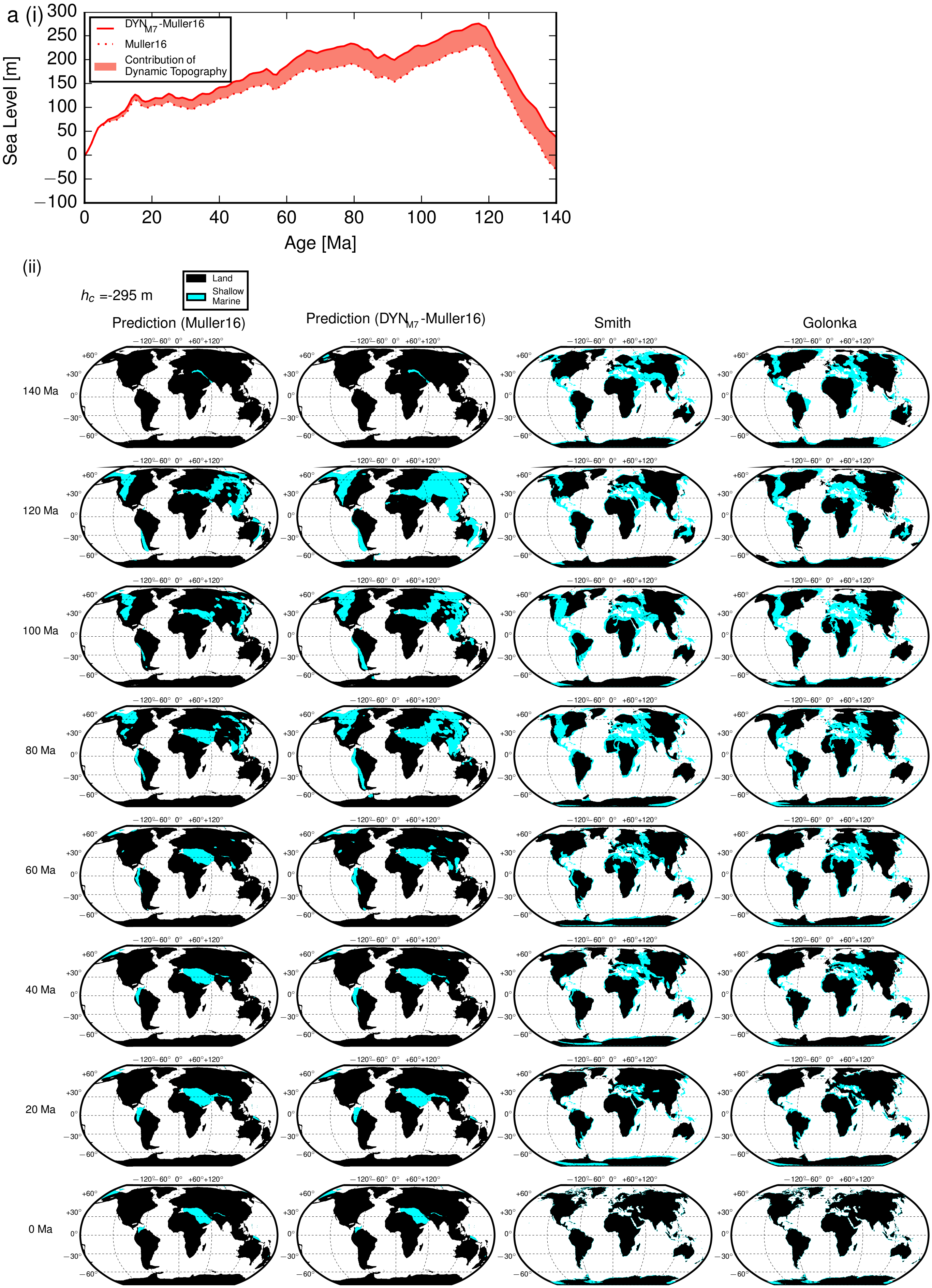

a (i)
DYN$_{M7}$-Muller16
Muller16
Contribution of Dynamic Topography
Sea Level [m]
Age [Ma]
(ii)
h_c =-295 m
Land
Shallow Marine
Prediction (Muller16)
Prediction (DYN$_{M7}$-Muller16)
Smith
Golonka
140 Ma
120 Ma
100 Ma
80 Ma
60 Ma
40 Ma
20 Ma
0 Ma

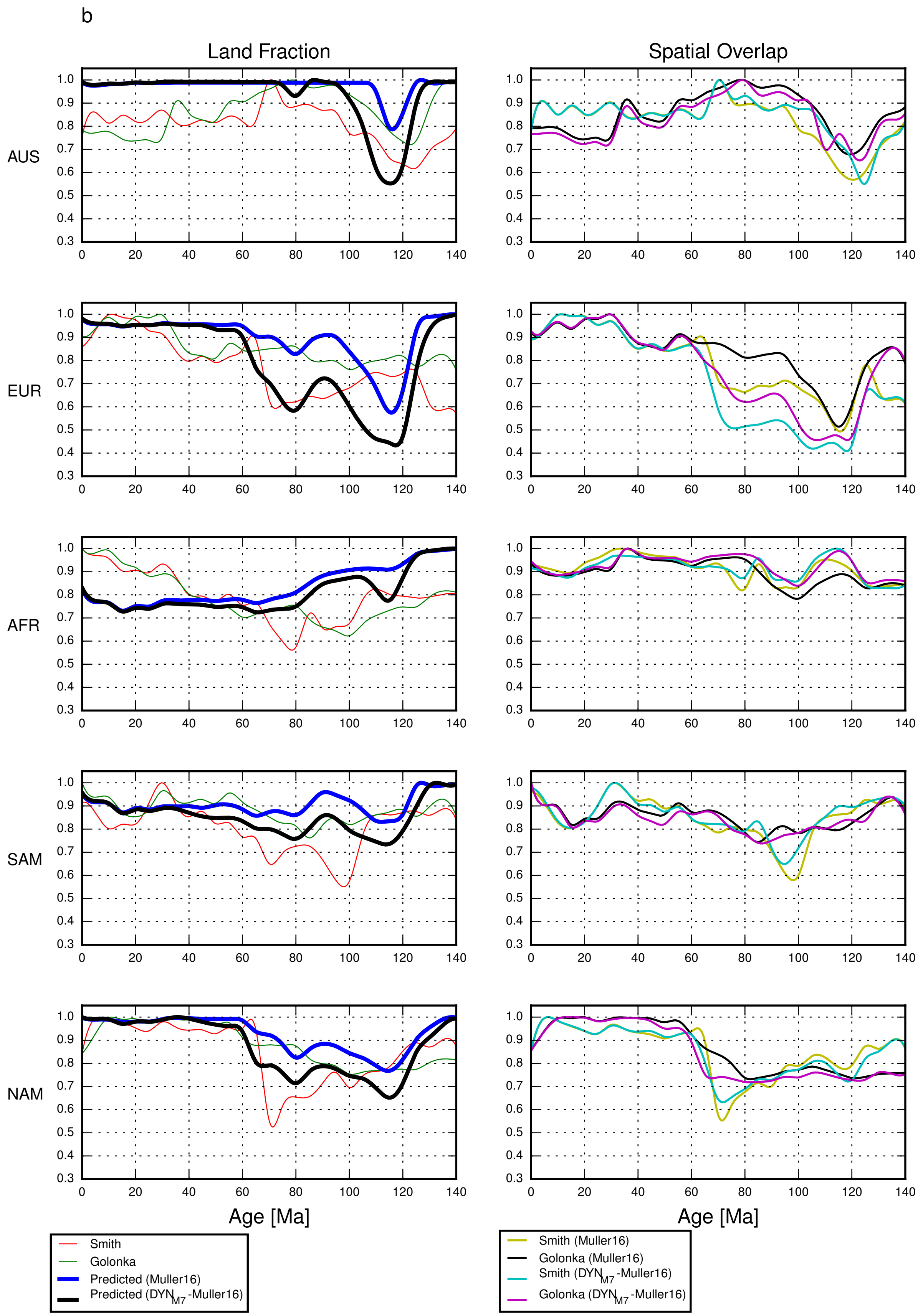
b
Land Fraction
Spatial Overlap
AUS
EUR
AFR
SAM
NAM
Age [Ma]
Age [Ma]
Smith
Golonka
Predicted (Muller16)
Predicted (DYN$_{M7}$-Muller16)
Smith (Muller16)
Golonka (Muller16)
Smith (DYN$_{M7}$-Muller16)
Golonka (DYN$_{M7}$-Muller16)

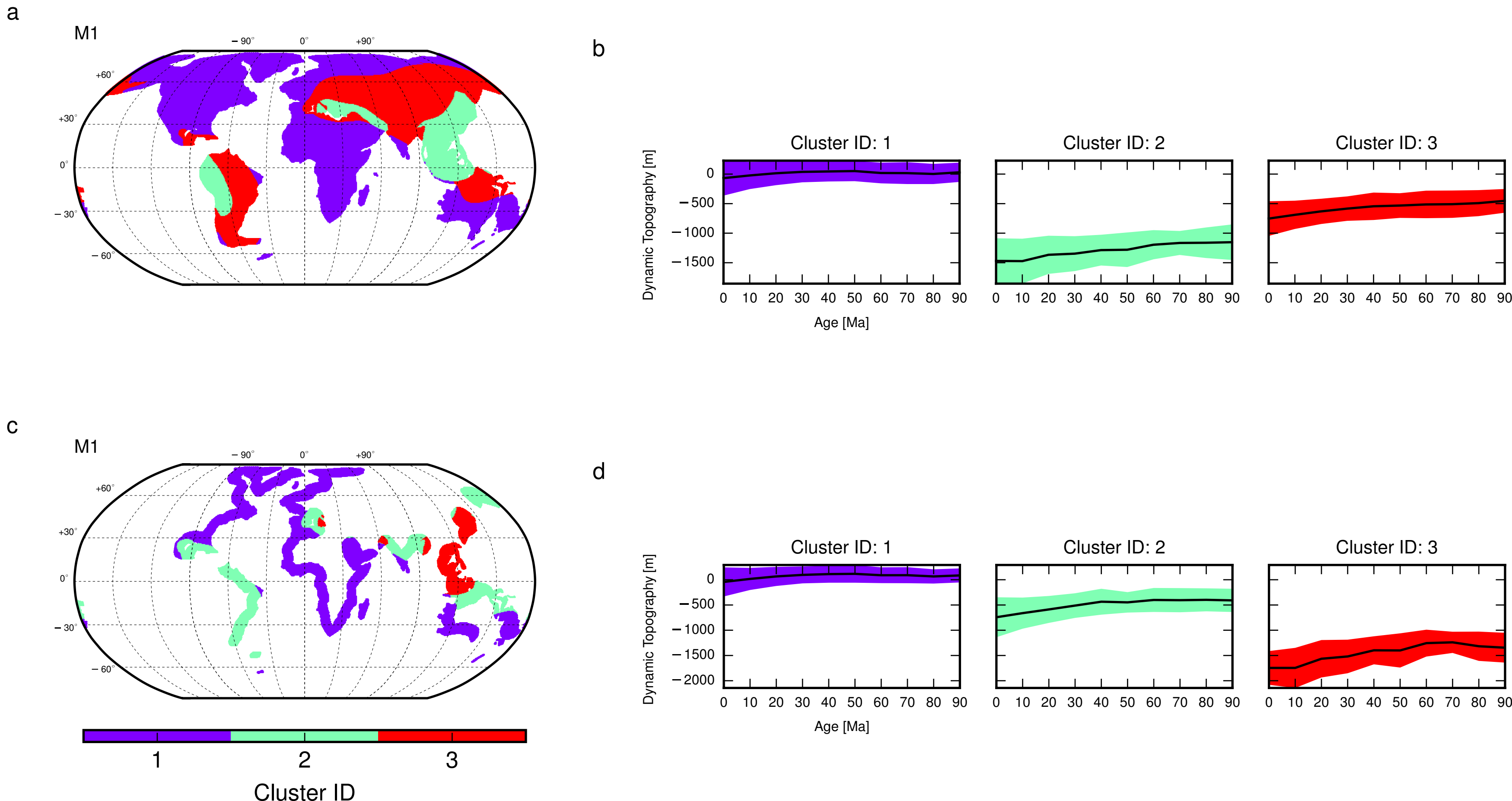
a
M1
− 90°
0°
+90°
+60°
+30°
0°
− 30°
− 60°
b
Cluster ID: 1
Cluster ID: 2
Cluster ID: 3
Dynamic Topography [m]
0
−500
−1000
−1500
0 10 20 30 40 50 60 70 80 90
Age [Ma]
c
M1
− 90°
0°
+90°
+60°
+30°
0°
− 30°
− 60°
d
Cluster ID: 1
Cluster ID: 2
Cluster ID: 3
Dynamic Topography [m]
0
−500
−1000
−1500
−2000
0 10 20 30 40 50 60 70 80 90
Age [Ma]
1
2
3
Cluster ID

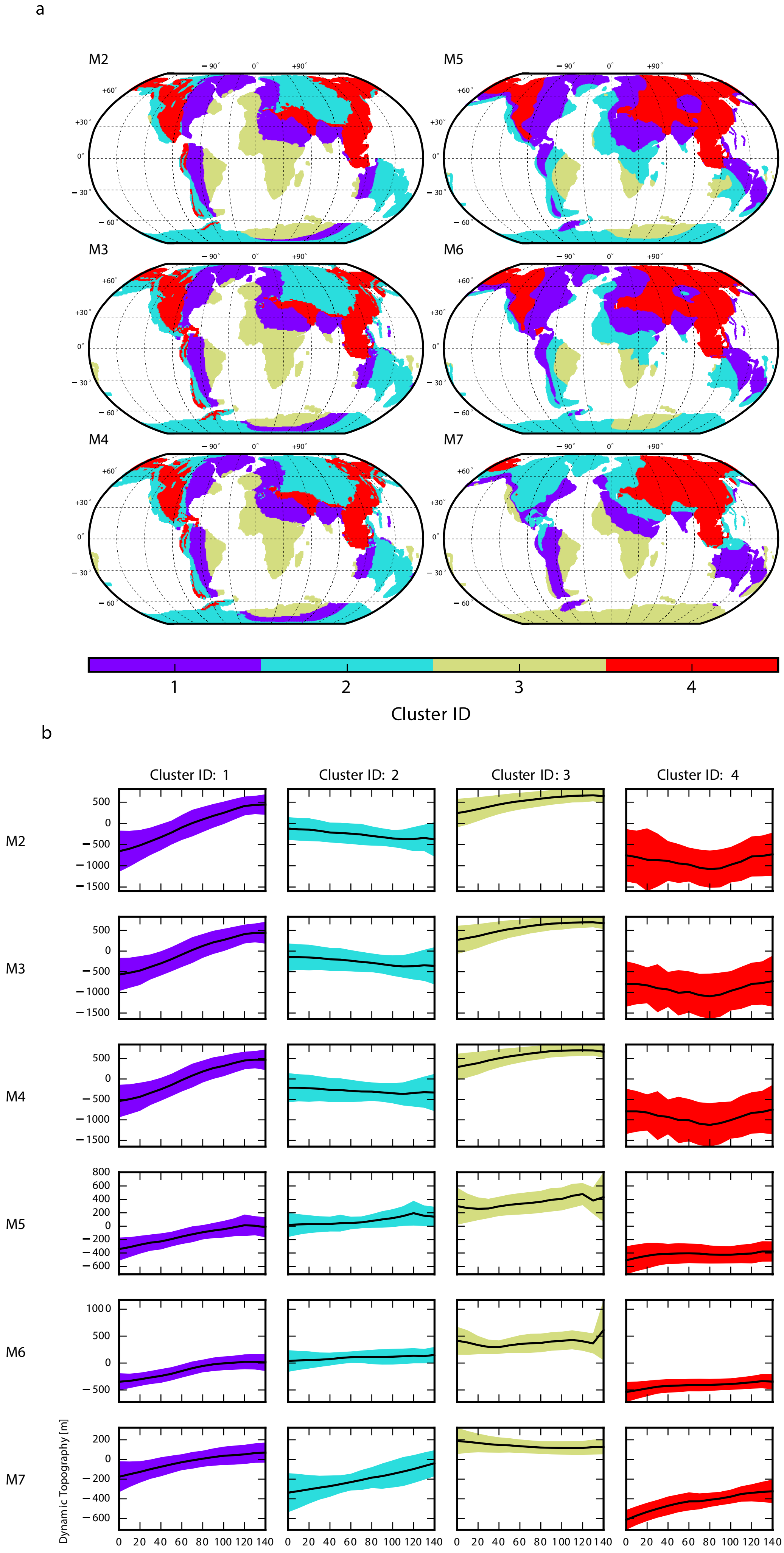
a
M2
M3
M4
M5
M6
M7
Cluster ID
1
2
3
4
b
Cluster ID: 1
Cluster ID: 2
Cluster ID: 3
Cluster ID: 4
Dynamic Topography [m]
Age [Ma]

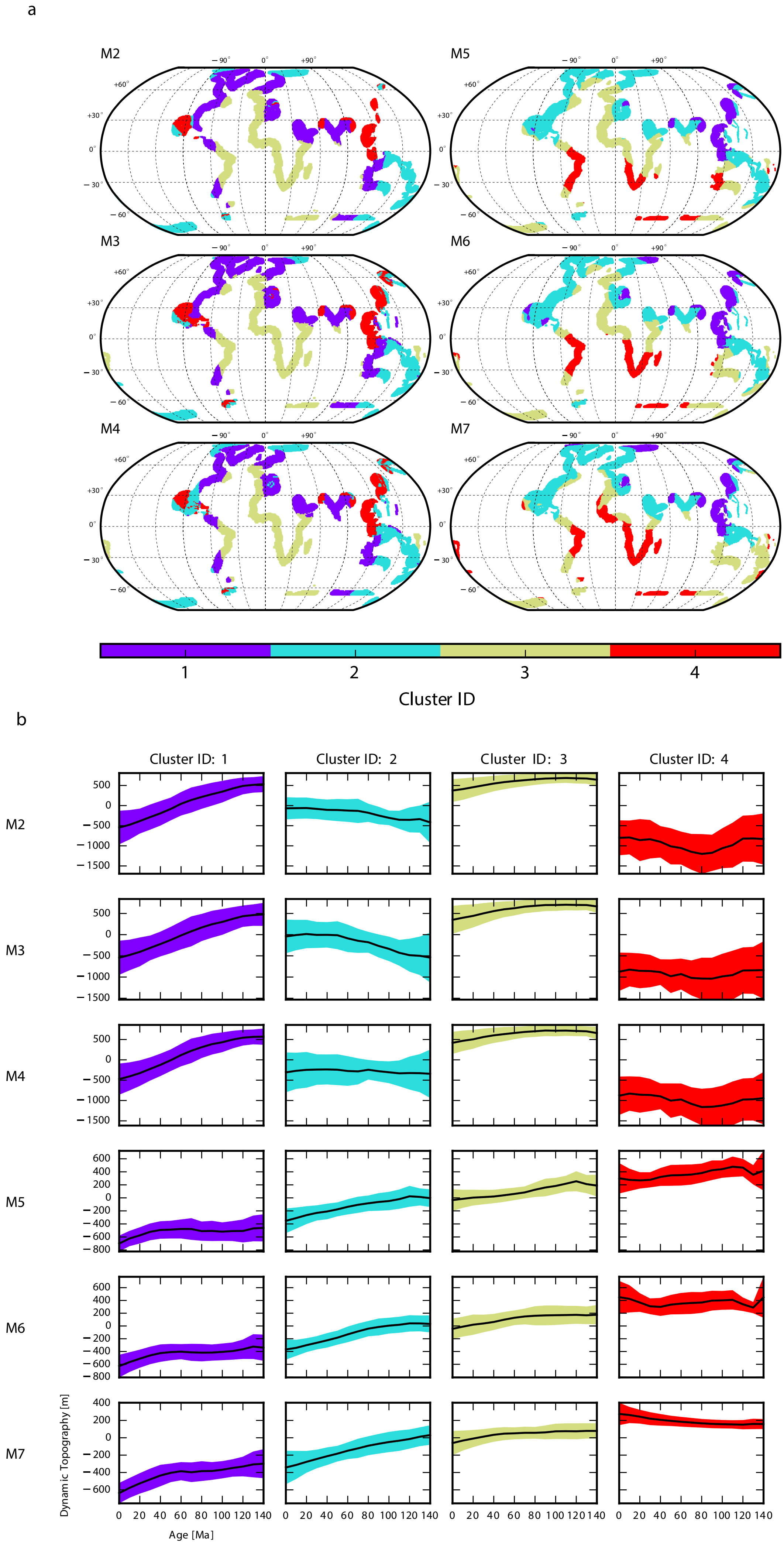

a
M2
M3
M4
M5
M6
M7
1
2
3
4
Cluster ID
b
Cluster ID: 1
Cluster ID: 2
Cluster ID: 3
Cluster ID: 4
Dynamic Topography [m]
Age [Ma]

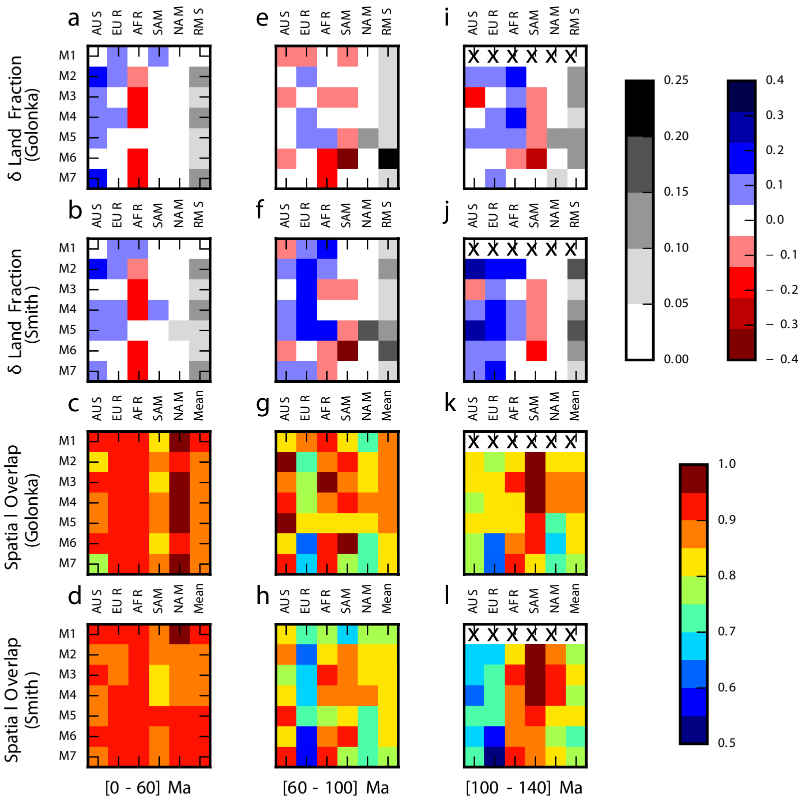

a
e
i
AUS
EUR
AFR
SAM
NAM
RMS
Mean
M1
M2
M3
M4
M5
M6
M7
δ Land Fraction (Golonka)
δ Land Fraction (Smith)
Spatial Overlap (Golonka)
Spatial Overlap (Smith)
b
f
j
c
g
k
d
h
l
0.25
0.20
0.15
0.10
0.05
0.00
0.4
0.3
0.2
0.1
0.0
− 0.1
− 0.2
− 0.3
− 0.4
1.0
0.9
0.8
0.7
0.6
0.5
[0 - 60] Ma
[60 - 100] Ma
[100 - 140] Ma

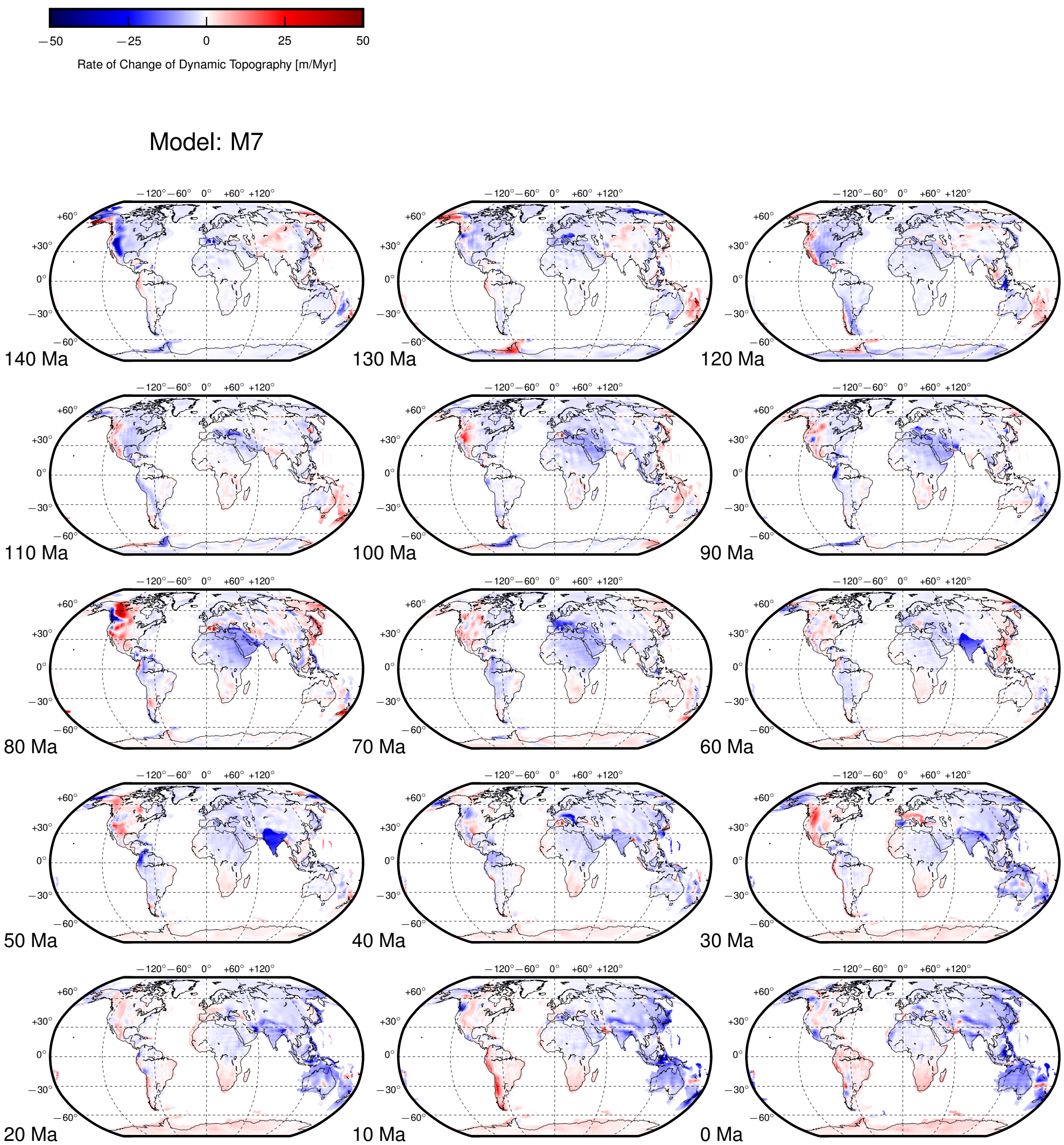

−50
−25
0
25
50
Rate of Change of Dynamic Topography [m/Myr]
Model: M7
140 Ma
130 Ma
120 Ma
110 Ma
100 Ma
90 Ma
80 Ma
70 Ma
60 Ma
50 Ma
40 Ma
30 Ma
20 Ma
10 Ma
0 Ma

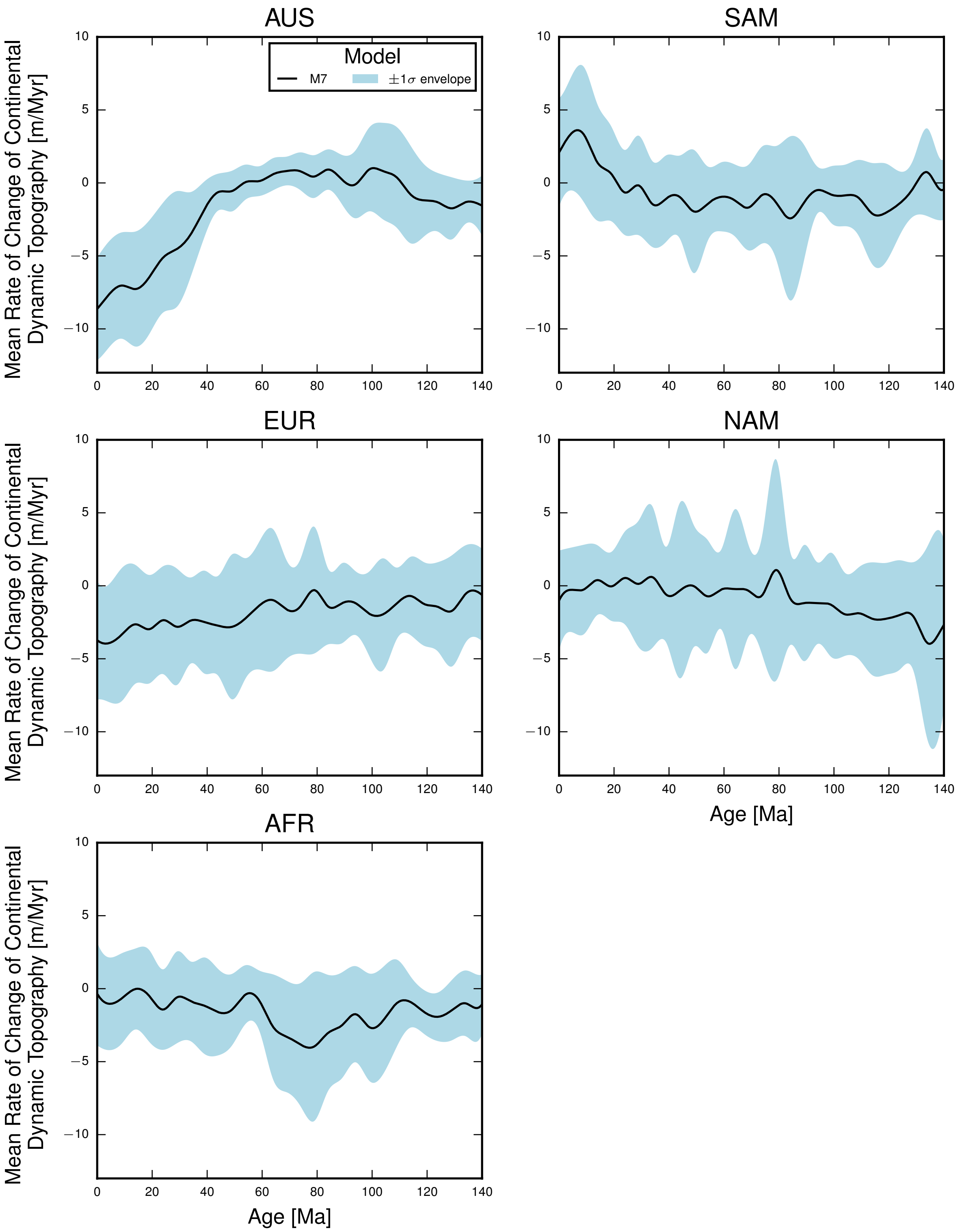
AUS
SAM
EUR
NAM
AFR
Model
M7
±1σ envelope
Mean Rate of Change of Continental Dynamic Topography [m/Myr]
Age [Ma]
10
5
0
−5
−10
0
20
40
60
80
100
120
140

Supplementary figures to "**Dynamic topography of passive continental margins and their hinterlands since the Cretaceous**" by R.D. Müller, R. Hassan, M. Gurnis, N. Flament, S.E. Williams.

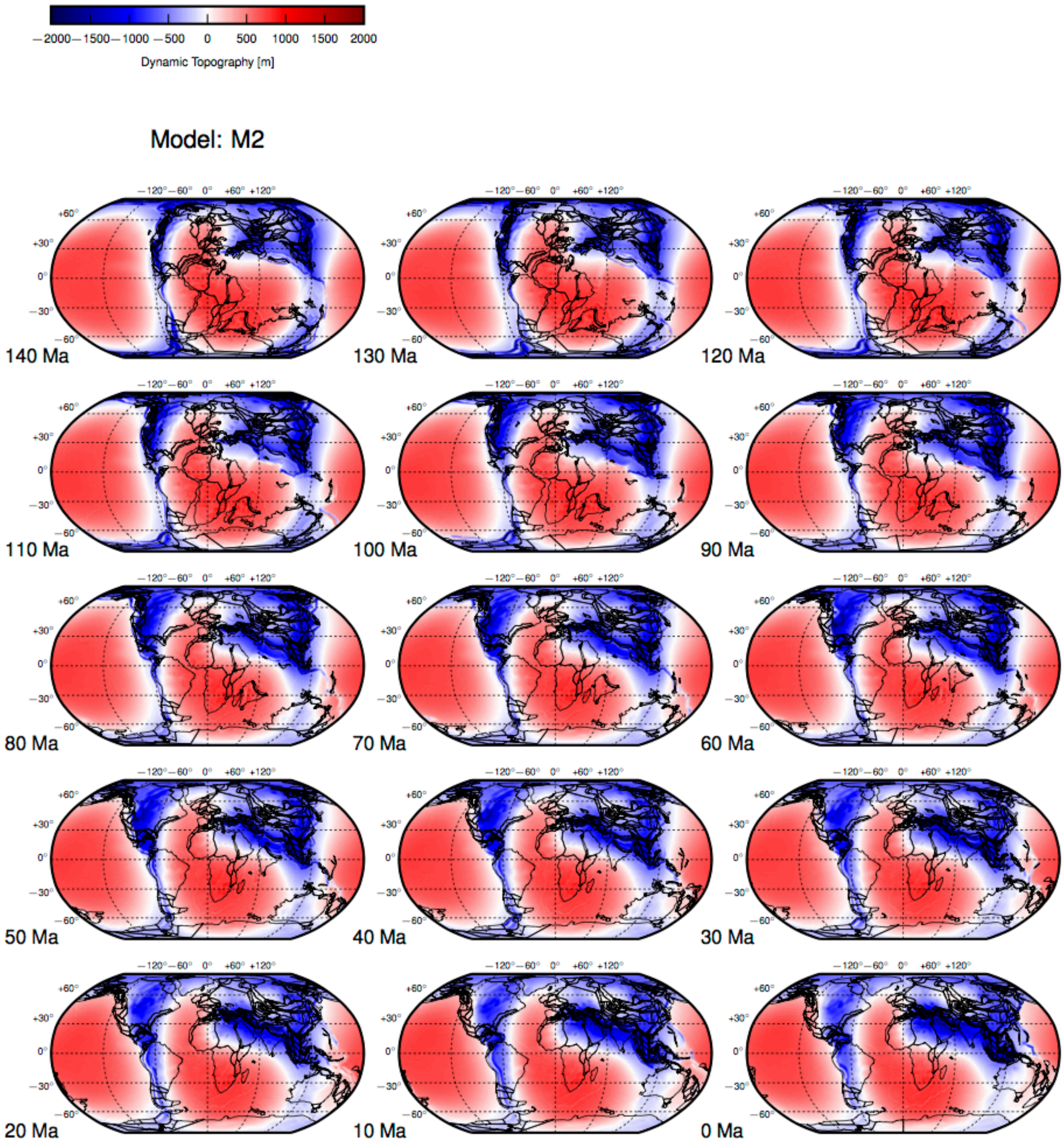

Supp. Fig. 1. Modelled dynamic topography in model M2 at 10 Myr intervals, with reconstructed continents (Seton et al., 2012) overlain.

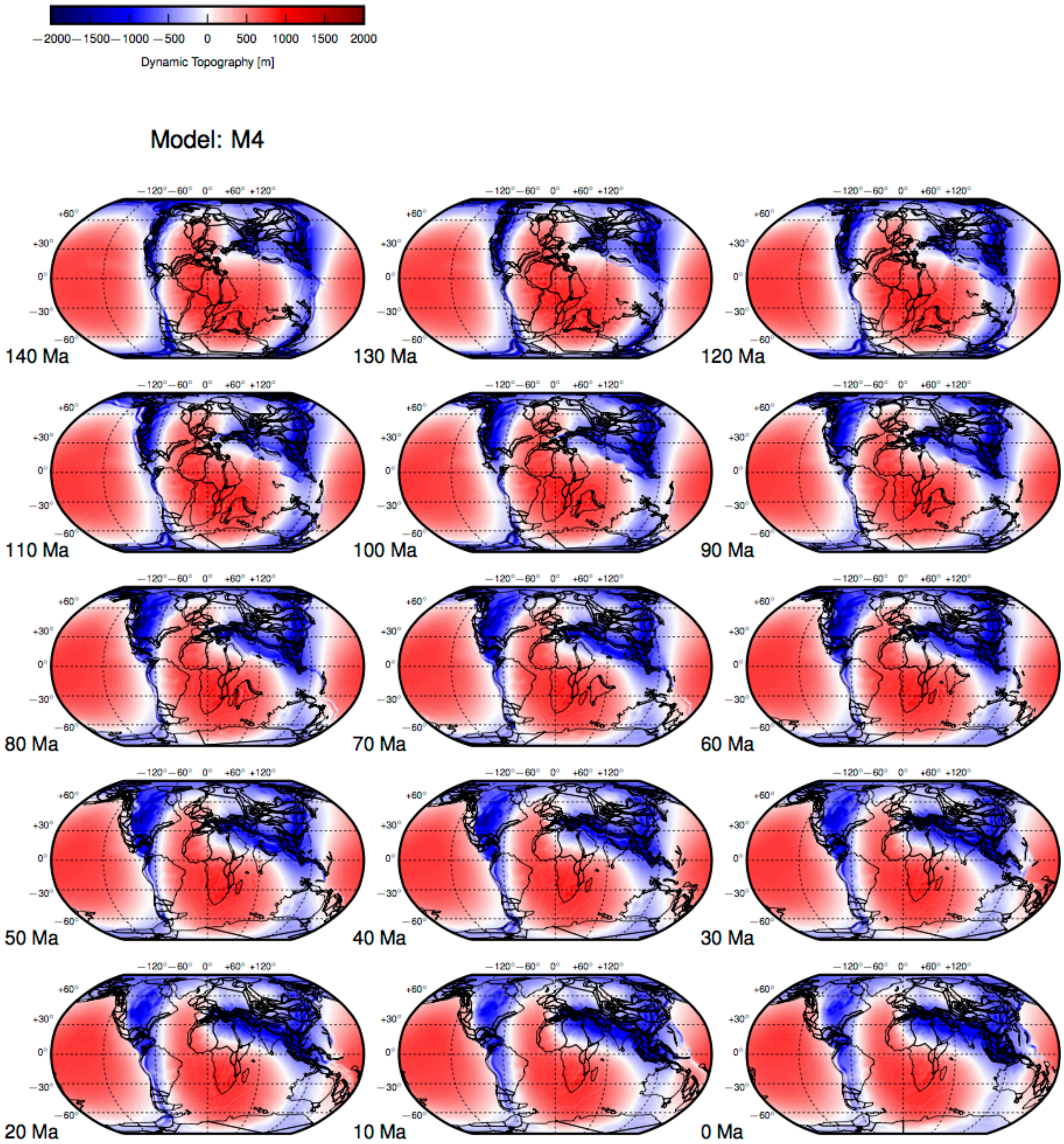

Supp. Fig. 2. Modelled dynamic topography in model M4 at 10 Myr intervals, with reconstructed continents (Van Der Meer et al., 2010) overlain.

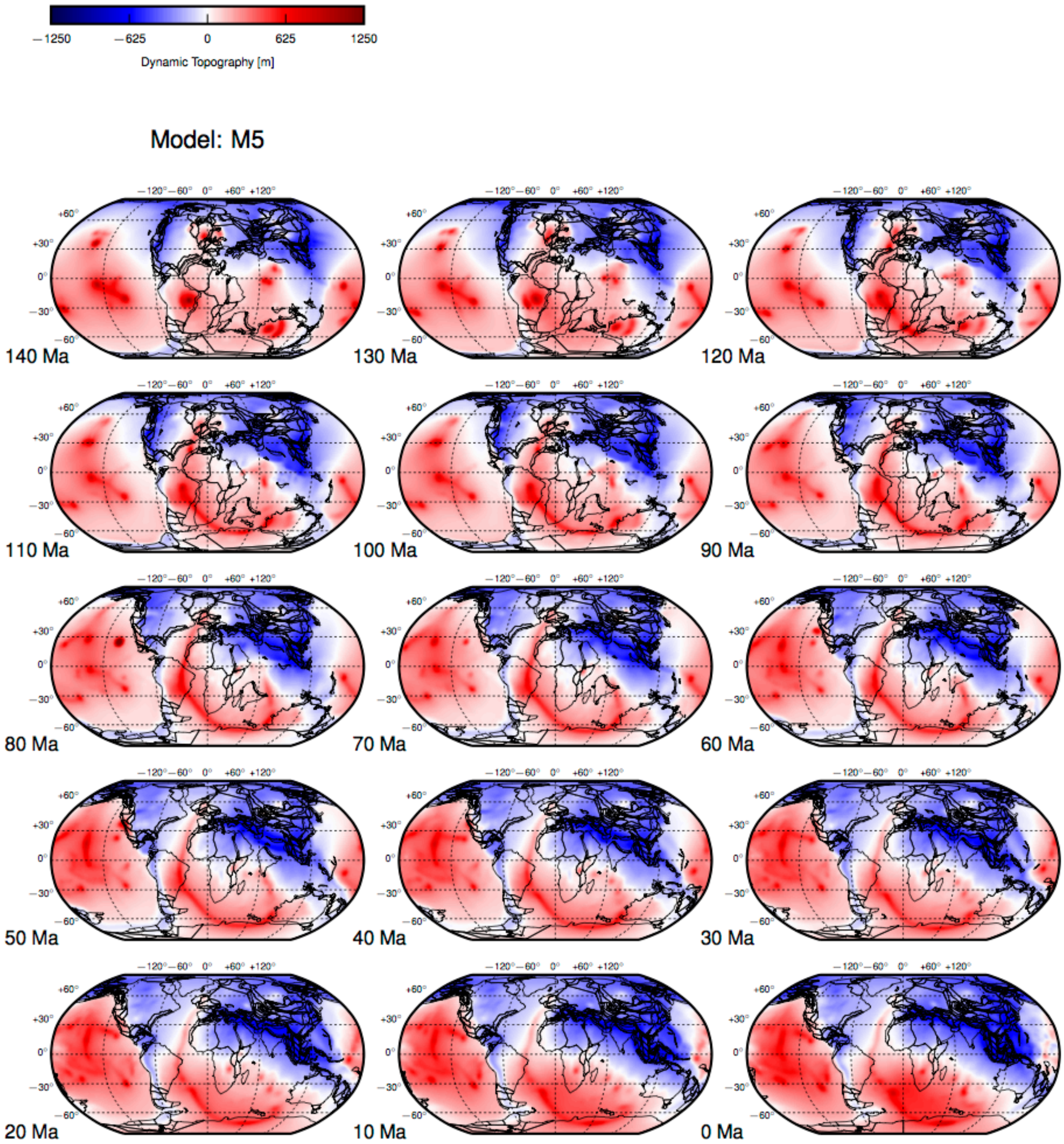

Supp. Fig. 3. Modelled dynamic topography in model M5 at 10 Myr intervals, with reconstructed continents (Seton et al., 2012) overlain.

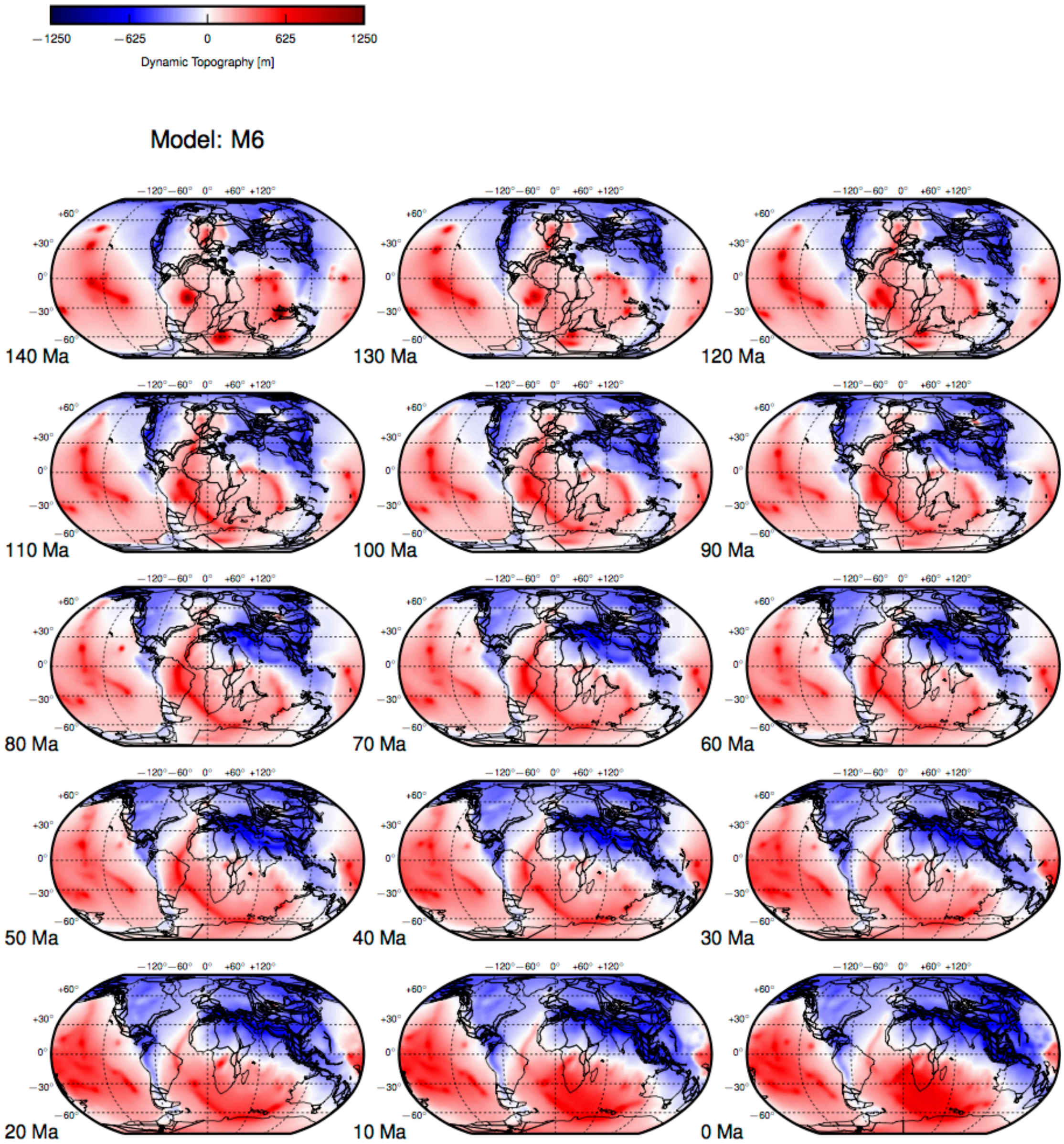

Supp. Fig. 4. Modelled dynamic topography in model M6 at 10 Myr intervals, with reconstructed continents (Müller et al., 2016) overlain.

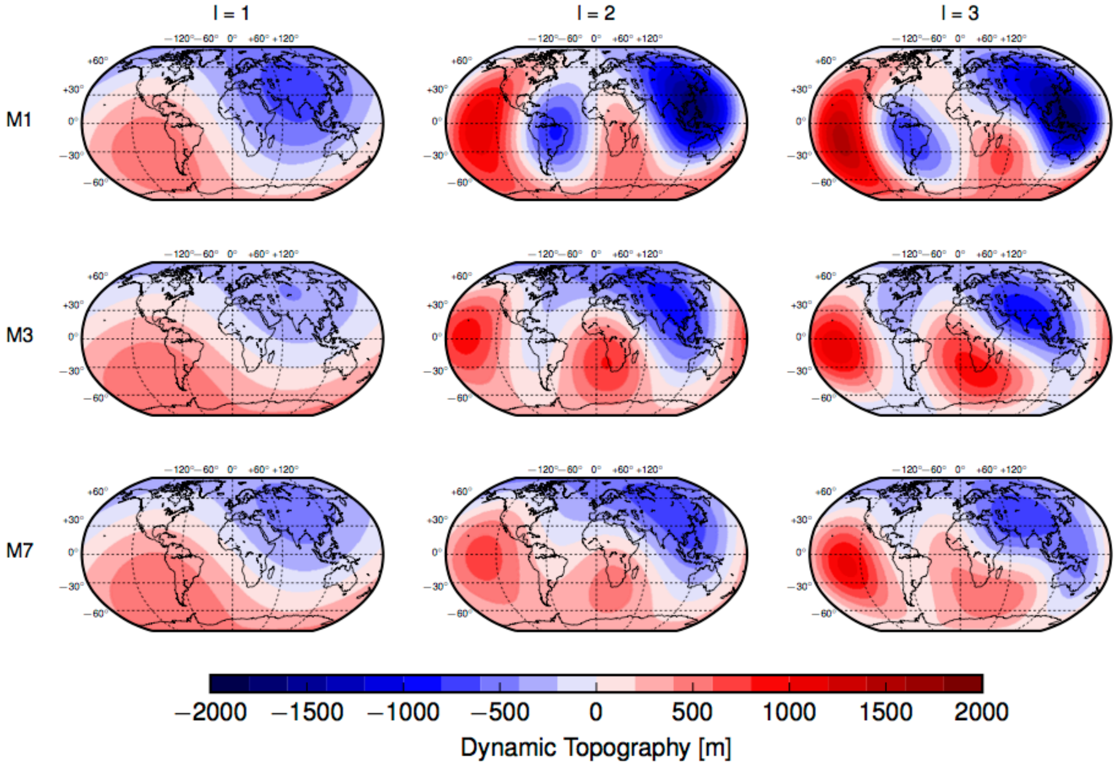

Supp. Fig. 5. Low-degree (1-3) spherical harmonic representations of present-day modelled dynamic topography in models M1, M3 and M7.

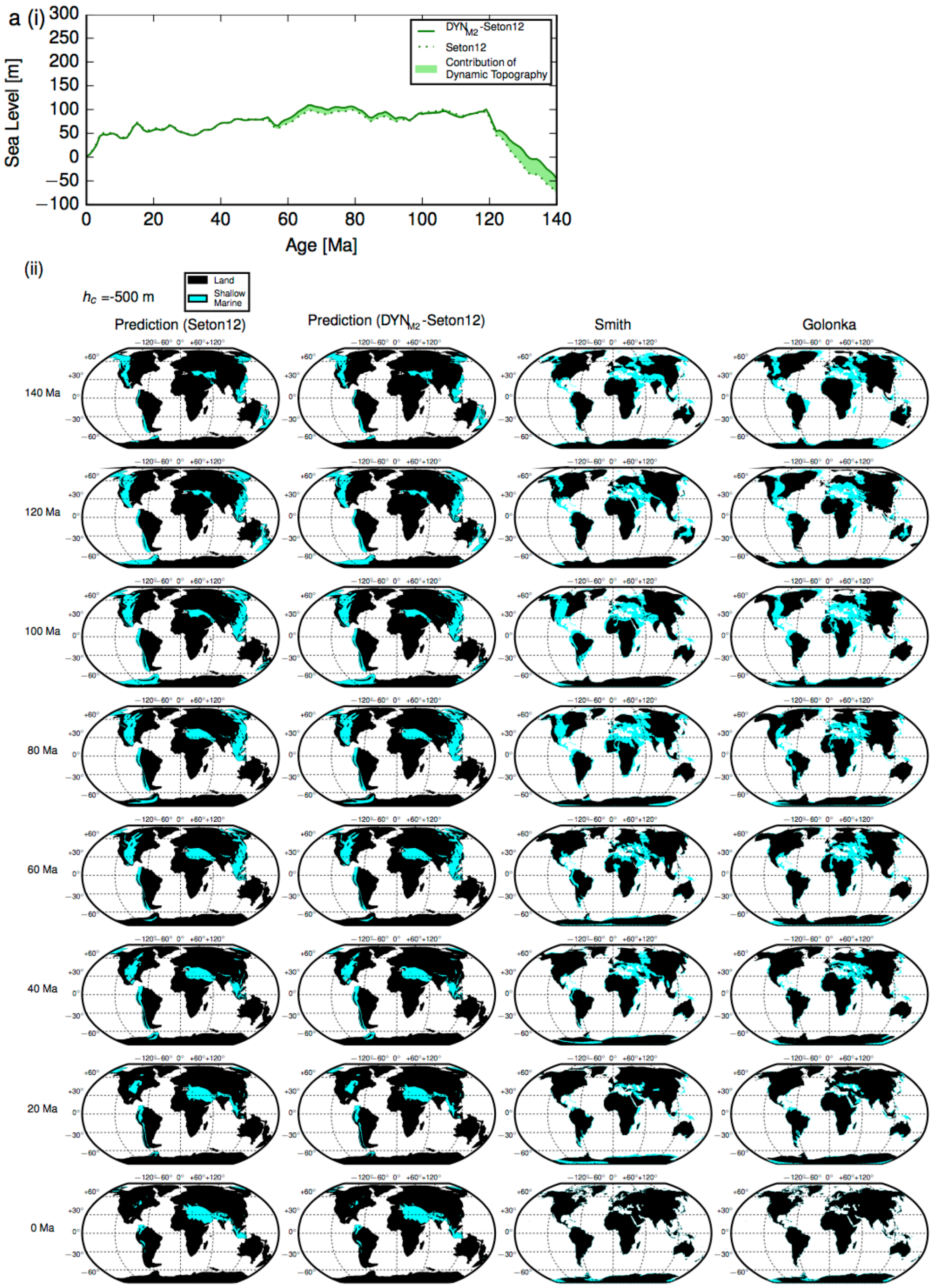

Supp. Fig. 6. (a) The distribution of oceans and continents predicted in model M2, based on the H87 long-term sea level curve, is shown in the first column at labelled ages (see methods for more details). The second column shows equivalent predictions based on the M16 sea level curve. The distribution of oceans and continents in the paleogeography models of Smith et al. (1994) and Golonka (2007, 2009) are shown in the third and fourth columns, respectively.

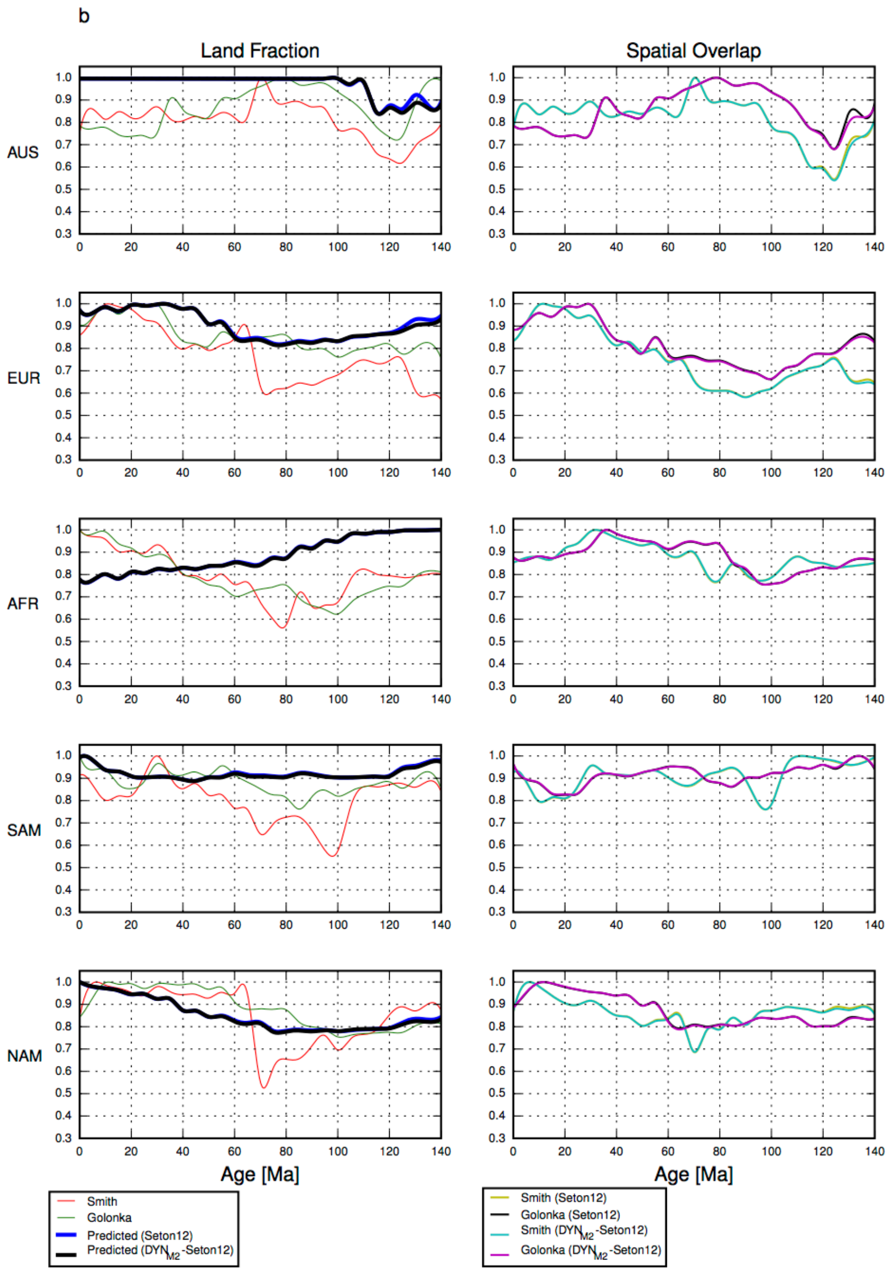

Supp. Fig. 6 (b). Evolution of the fraction of land, $\tau(t)$, over the last 140 Ma as predicted in model M2, based on sea level curves H87 (blue) and M16 (black) are shown on the first column for each labelled continent. Evolution of the fraction of land, $\tau(t)$, computed for paleogeography grids from Smith et al. (1994) and Golonka (2007, 2009) are also shown in red and green, respectively, for labelled ages in the first column. The yellow and black curves in the second column show the evolution of spatial overlap, $\mu(t)$, (see methods) between predictions of inundation patterns within each continent in model M2, based on sea level curve H87, and those from paleogeography grids of Smith et al. (1994) and Golonka (2007, 2009), respectively. The cyan and magenta curves show the equivalent result, but for sea level curve M16.

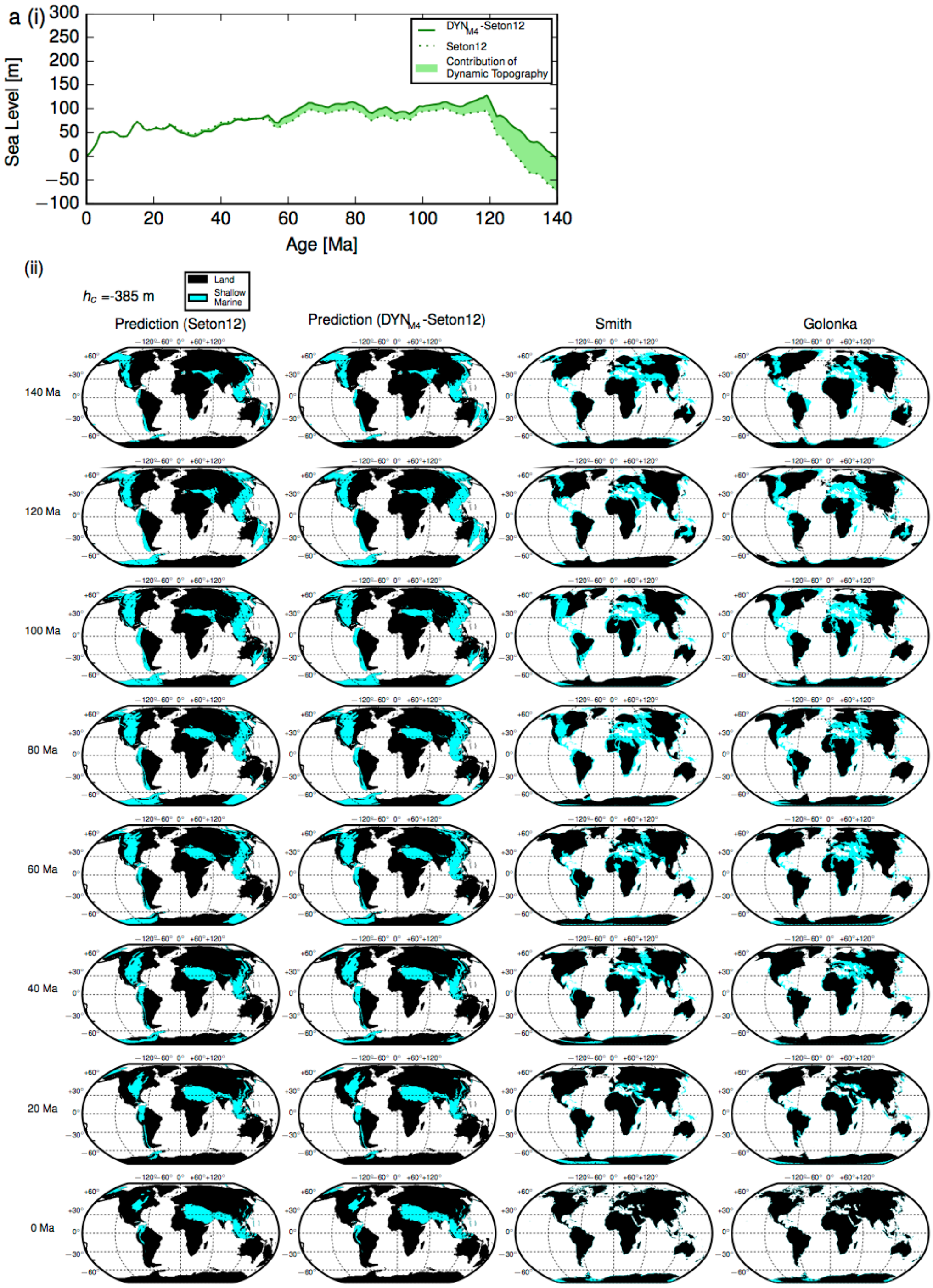

Supp. Fig. 7. (a) The distribution of oceans and continents predicted in model M4, based on the H87 long-term sea level curve, is shown in the first column at labelled ages (see methods for more details). The second column shows equivalent predictions based on the M16 sea level curve. The distribution of oceans and continents in the paleogeography models of Smith et al. (1994) and Golonka (2007, 2009) are shown in the third and fourth columns, respectively.

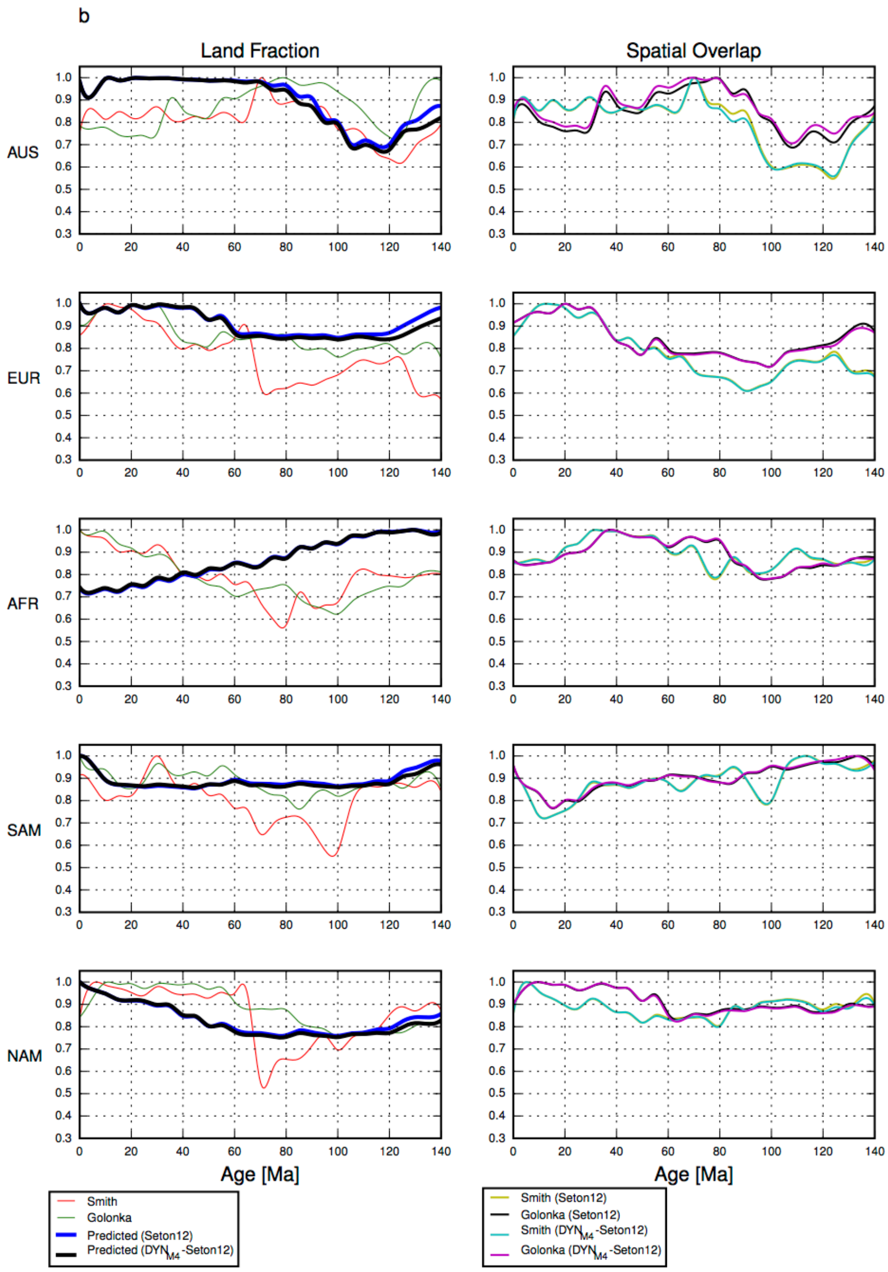

Supp. Fig. 7 (b). Evolution of the fraction of land, $\tau(t)$, over the last 140 Ma as predicted in model M4, based on sea level curves H87 (blue) and M16 (black) are shown on the first column for each labelled continent. Evolution of the fraction of land, $\tau(t)$, computed for paleogeography grids from Smith et al. (1994) and Golonka (2007, 2009) are also shown in red and green, respectively, for labelled ages in the first column. The yellow and black curves in the second column show the evolution of spatial overlap, $\mu(t)$, (see methods) between predictions of inundation patterns within each continent in model M4, based on sea level curve H87, and those from paleogeography grids of Smith et al. (1994) and Golonka (2007, 2009), respectively. The cyan and magenta curves show the equivalent result, but for sea level curve M16.

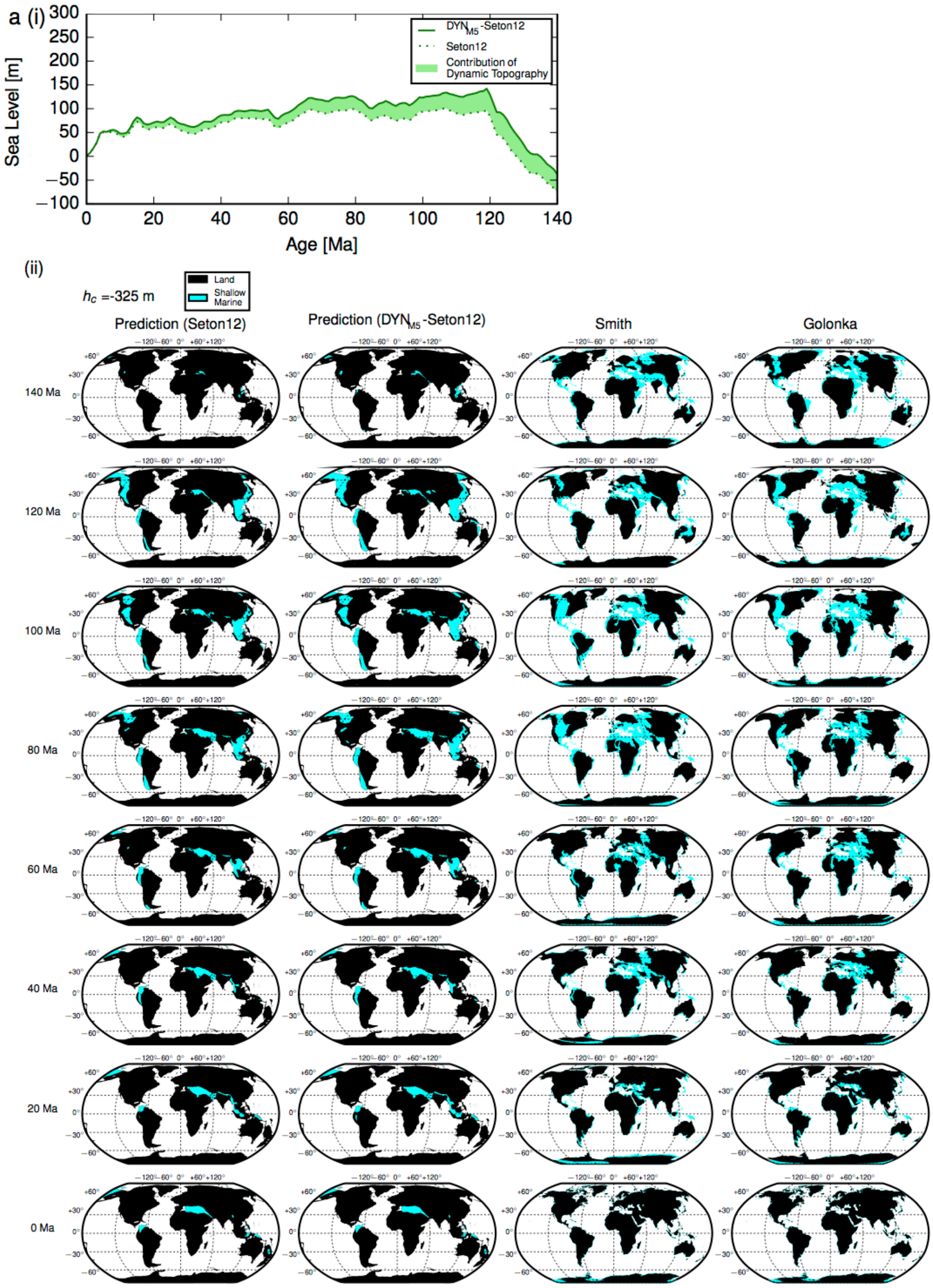

Supp. Fig. 8. (a) The distribution of oceans and continents predicted in model M5, based on the H87 long-term sea level curve, is shown in the first column at labelled ages (see methods for more details). The second column shows equivalent predictions based on the M16 sea level curve. The distribution of oceans and continents in the paleogeography models of Smith et al. (1994) and Golonka (2007, 2009) are shown in the third and fourth columns, respectively.

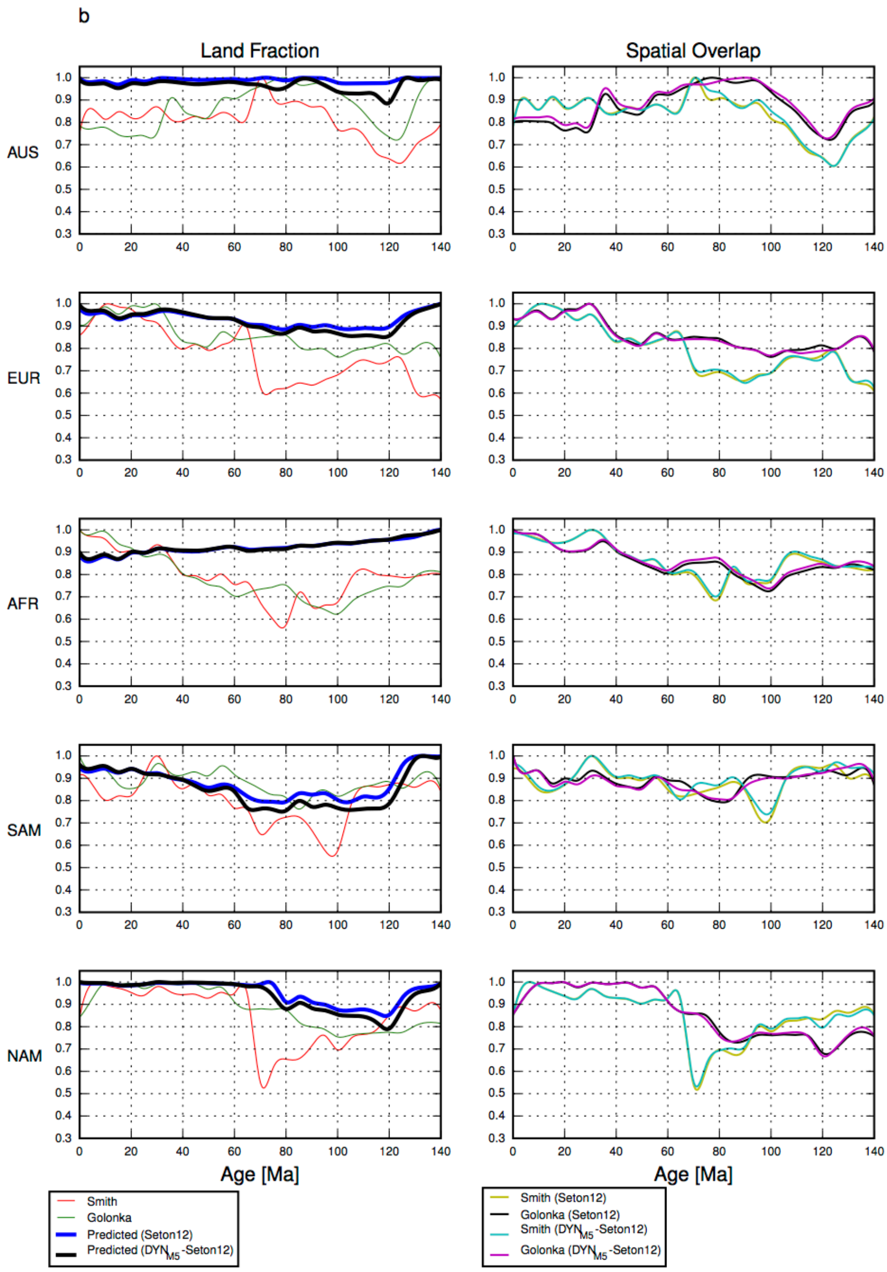

Supp. Fig. 8 (b). Evolution of the fraction of land, $\tau(t)$, over the last 140 Ma as predicted in model M5, based on sea level curves H87 (blue) and M16 (black) are shown on the first column for each labelled continent. Evolution of the fraction of land, $\tau(t)$, computed for paleogeography grids from Smith et al. (1994) and Golonka (2007, 2009) are also shown in red and green, respectively, for labelled ages in the first column. The yellow and black curves in the second column show the evolution of spatial overlap, $\mu(t)$, (see methods) between predictions of inundation patterns within each continent in model M5, based on sea level curve H87, and those from paleogeography grids of Smith et al. (1994) and Golonka (2007, 2009), respectively. The cyan and magenta curves show the equivalent result, but for sea level curve M16.

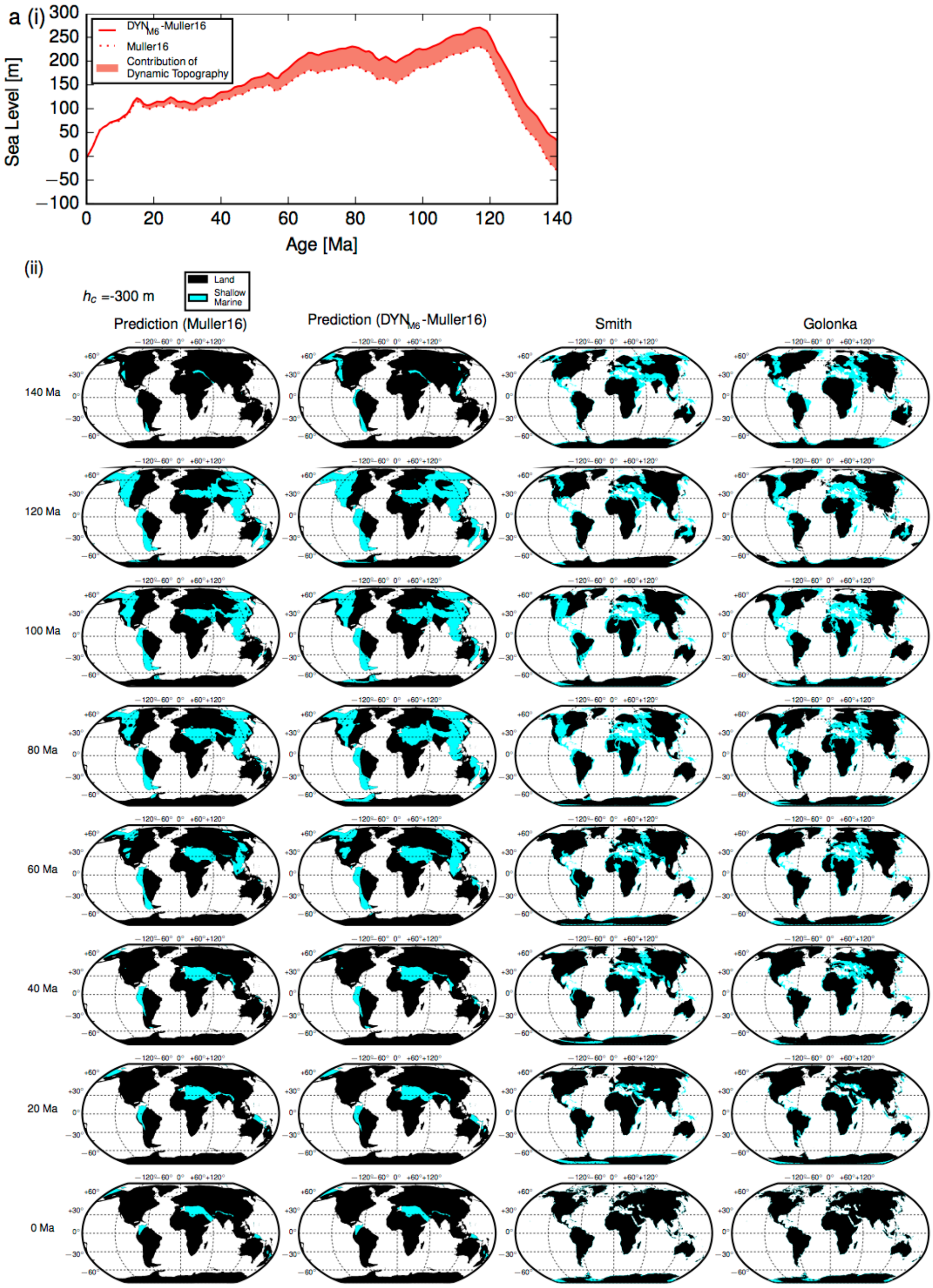

Supp. Fig. 9 (a). The distribution of oceans and continents predicted in model M6, based on the H87 long-term sea level curve, is shown in the first column at labelled ages (see methods for more details). The second column shows equivalent predictions based on the M16 sea level curve. The distribution of oceans and continents in the paleogeography models of Smith et al. (1994) and Golonka (2007, 2009) are shown in the third and fourth columns, respectively.

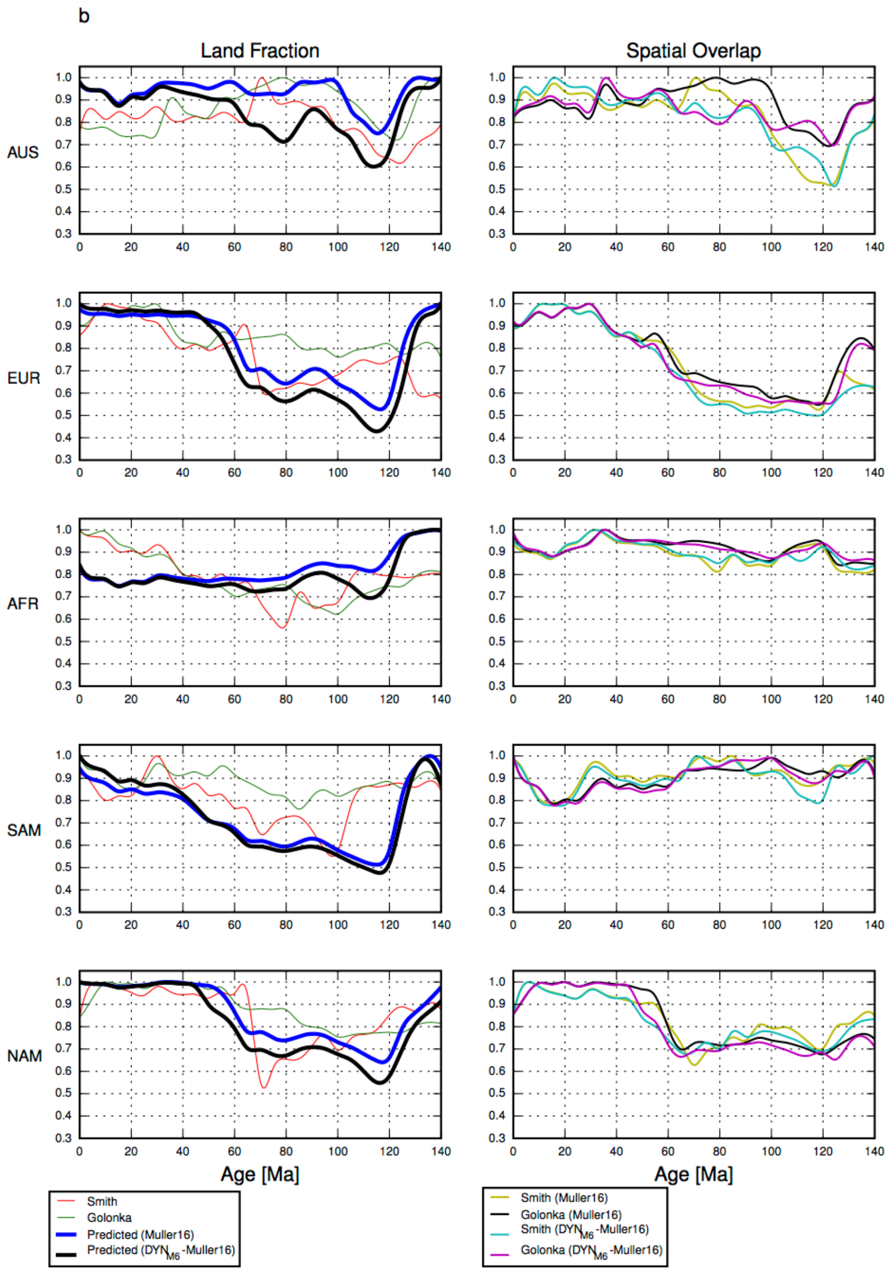

Supp. Fig. 9 (b). Evolution of the fraction of land, $\tau(t)$, over the last 140 Ma as predicted in model M6, based on sea level curves H87 (blue) and M16 (black) are shown on the first column for each labelled continent. Evolution of the fraction of land, $\tau(t)$, computed for paleogeography grids from Smith et al. (1994) and Golonka (2007, 2009) are also shown in red and green, respectively, for labelled ages in the first column. The yellow and black curves in the second column show the evolution of spatial overlap, $\mu(t)$, (see methods) between predictions of inundation patterns within each continent in model M6, based on sea level curve H87, and those from paleogeography grids of Smith et al. (1994) and Golonka (2007, 2009), respectively. The cyan and magenta curves show the equivalent result, but for sea level curve M16.

References

Golonka, J., 2007. Phanerozoic paleoenvironment and paleolithofacies maps: Mesozoic. Geologia/Akademia Górniczo-Hutnicza im. Stanisława Staszica w Krakowie 33, 211-264.

Golonka, J., 2009. Phanerozoic paleoenvironment and paleolithofacies maps: Cenozoic. Geologia/Akademia Górniczo-Hutnicza im. Stanisława Staszica w Krakowie 35, 507-587.

Müller, R.D., Seton, M., Zahirovic, S., Williams, S.E., Matthews, K.J., Wright, N.M., Shephard, G., Maloney, K.T., Barnett-Moore, N., Hosseinpour, M., Bower, D.J., Cannon, J., 2016. Ocean basin evolution and global-scale plate reorganization events since Pangea breakup. Annual Review of Earth and Planetary Sciences 44, 107-138.

Seton, M., Muller, R.D., Zahirovic, S., Gaina, C., Torsvik, T.H., Shephard, G., Talsma, A., Gurnis, M., Turner, M., Maus, S., Chandler, M.T., 2012. Global continental and ocean basin reconstructions since 200 Ma. Earth Science Reviews 113, 212-270.

Smith, A.G., Smith, D.G., Funnell, B.M., 1994. Atlas of Mesozoic and Cenozoic Coastlines. Cambridge University Press, Cambridge.

Van Der Meer, D.G., Spakman, W., Van Hinsbergen, D.J., Amaru, M.L., Torsvik, T.H., 2010. Towards absolute plate motions constrained by lower-mantle slab remnants. Nature Geoscience 3, 36-40.